Article

The Balance of Prickle/Spiny-Legs Isoforms Controls the Amount of Coupling between Core and Fat PCP Systems

Matthias Merkel,[1,3] Andreas Sagner,[2,3]
Franz Sebastian Gruber,[2] Raphael Etournay,[2]
Corinna Blasse,[2] Eugene Myers,[2] Suzanne Eaton,[2,*]
and Frank Jülicher[1,*]
[1]Max Planck Institute for the Physics of Complex Systems,
Nöthnitzer Strasse 38, 01187 Dresden, Germany
[2]Max Planck Institute of Molecular Cell Biology and Genetics,
Pfotenhauerstrasse 108, 01309 Dresden, Germany

Summary

Background: The conserved Fat and Core planar cell polarity (PCP) pathways work together to specify tissue-wide orientation of hairs and ridges in the *Drosophila* wing. Their components form intracellularly polarized complexes at *adherens* junctions that couple the polarity of adjacent cells and form global patterns. How Fat and Core PCP systems interact is not understood. Some studies suggest that Fat PCP directly orients patterns formed by Core PCP components. Others implicate oriented tissue remodeling in specifying Core PCP patterns.
Results: We use genetics, quantitative image analysis, and physical modeling to study Fat and Core PCP interactions during wing development. We show their patterns change during morphogenesis, undergoing phases of coupling and uncoupling that are regulated by antagonistic Core PCP protein isoforms Prickle and Spiny-legs. Evolving patterns of Core PCP are hysteretic: the early Core PCP pattern is modified by tissue flows and then by coupling to Fat PCP, producing sequential patterns that guide hairs and then ridges. Our data quantitatively account for altered hair and ridge polarity patterns in PCP mutants. Premature coupling between Fat and Core PCP explains altered polarity patterns in *pk* mutants. In other Core PCP mutants, hair polarity patterns are guided directly by Fat PCP. When both systems fail, hairs still align locally and obey signals associated with veins.
Conclusions: Temporally regulated coupling between the Fat and Core PCP systems enables a single tissue to develop sequential polarity patterns that orient distinct morphological structures.

Introduction

Planar cell polarity (PCP) underlies coordinated cell behaviors that organize developing tissues [1]. It orients the cell divisions and rearrangements that specify tissue shape and coordinates tissue shape with the global alignment of external structures such as hairs and cilia. Planar polarity in the *Drosophila* wing is reflected in its growth orientation (biased along the proximo-distal [PD] axis) [2, 3], in the uniform distal orientation of wing hairs [4], and in a more complex pattern of cuticular ridges formed by wing epithelial cells [5]. The wing develops from a folded epithelial sac, or imaginal disc. Discs grow during larval

development, and after pupariation they undergo morphogenetic movements that oppose the dorsal and ventral wing surfaces [6], refine wing shape [7], and regularize its packing geometry [8]. Wing hairs emerge about 30 hr after puparium formation (hAPF), and adult cuticle secretion begins shortly afterward.

Planar polarized features of wing development are influenced by two different molecular systems, termed Core PCP and Fat PCP [1, 9]. Both consist of proteins that form asymmetric complexes at cell junctions that couple the polarity of adjacent cells and develop tissue-wide polarity patterns [10–13]. Perturbing each pathway produces distinct alterations in hair and ridge orientation [4, 5, 14, 15]. Fat PCP also influences growth orientation in the larval wing [2, 3]. How global patterns of Fat and Core PCP emerge and the functional relationship between them is not completely understood.

One-half of the Core PCP complex is composed of the seven-pass transmembrane cadherin Flamingo (Fmi), the seven-pass transmembrane protein Frizzled (Fz), and the peripherally associated proteins Dishevelled and Diego. These interact across *adherens* junctions with a complementary complex in the adjacent cell consisting of Fmi, the transmembrane protein Strabismus (Stbm), and a peripherally associated protein derived from the *prickle* locus [1, 9]. Two protein isoforms produced by this locus, Prickle (Pk) and Spiny-legs (Sple), differ in their N terminus and are required tissue specifically [16]. Core PCP complexes with opposite polarities segregate to different sides of the cell, generating intracellular polarity that is coupled between neighbors. Global patterns of Core PCP emerge during larval growth and change dynamically during wing morphogenesis [7, 8, 12, 17]. At the time hairs form, Core PCP complexes are uniformly aligned along the PD axis of the wing with Fz-containing domains facing distally [1, 9]. Loss of Core PCP components causes reproducible changes in the hair pattern: hair polarity throughout the wing has a strong anterior-posterior (AP) component and tends to point either toward or away from the third wing vein (L3), depending on the specific mutation [4, 15].

Positive and negative interactions between Core PCP proteins within and between cells appear to self-organize polarity and align it between small groups of cells. Global Core PCP patterns are thought to rely on cues that bias the direction of the feedback interactions. The Fat system has been proposed to be one such cue [9], and genetic evidence for its involvement is strongest for tissues and structures whose polarity depends on Sple [15, 18–20]. However, Fat and Core PCP can also operate independently to orient hairs and bristles [21, 22]. In the wing, distal hair orientation depends on Pk and not on Sple [16]. Nonetheless, loss of Fat PCP perturbs hair polarity in the proximal wing blade [14]. How it does so is controversial.

The Fat PCP system is based on the atypical cadherins Fat (Ft) and Dachsous (Ds), which bind heterophilically across cell contacts, and the Golgi-kinase Four-jointed (Fj), which modulates their affinities for each other [23, 24]. Intracellular asymmetry of Ft:Ds heterodimers is established in response to opposing tissue-wide expression gradients of *ds* and *fj* such that intracellular Ds polarity points down the Ds gradient

[3]Co-first author
*Correspondence: eaton@mpi-cbg.de (S.E.), julicher@pks.mpg.de (F.J.)

[10–12]. Fat:Ds heterodimer polarity causes intracellular polarization of the atypical myosin Dachs [3, 25]. In the larval wing disc, Fat PCP vectors, which we define as pointing toward the side of the cell that accumulates Ds and Dachs, are aligned with growth orientation, pointing in a roughly radial pattern toward the center of the wing pouch. This pattern is similar to that of Core PCP vectors (with Ds and Fz orienting the same direction) [12, 17]. However, Fat PCP vectors (deduced from transcriptional gradients of Fj and Ds) point opposite to Core PCP in the eye and have the opposite relationship to hair and bristle polarity in the anterior abdomen [9, 26–28].

Despite the similarity of their patterns in larval wing discs, Fat PCP influences the disc Core pattern only near the presumptive hinge; elsewhere, it is guided by signals from the AP and dorsoventral (DV) compartment boundaries [17]. After pupariation, Core PCP reorganizes to form a fan-shaped pattern. Later, during pupal morphogenesis, it reorients distally, forming the pattern that guides wing hair outgrowth [7]. Whether Fat PCP orientation changes similarly during pupal development has never been examined, and the functional relationship between the two pathways at this stage is unclear. Distal realignment of Core PCP depends on oriented epithelial remodeling that reshapes the wing blade at this time. Gain and loss of cell contacts that are biased in the PD axis, along with PD cell elongation, suffice to shift the Core PCP axis in simulations [7]. However, epithelial remodeling also coincides with PD alignment of microtubules, which is perturbed in Fat pathway mutants and has been proposed to bias transport of Fz-containing vesicles [29, 30].

Here, we have sought to clarify the functional relationship between the Fat PCP and Core PCP systems in the wing. We quantify and compare their global patterns of polarity throughout development, examine how these systems influence each other's polarity, and probe their respective functions in hair and ridge orientation.

Results

Core PCP and Ft PCP Patterns Diverge during Pupal Wing Remodeling

To investigate the relationship of Fat and Core PCP systems, we quantified and compared their polarity patterns throughout wing development. Previous studies showed that their patterns in the larval wing pouch are similar near the interface between hinge and blade regions [12, 17]. In the central wing pouch, the Core PCP pattern is oriented with respect to the DV and AP compartment boundaries, but Dachs::V5-expressing clones did not reveal strong Fat system polarity in this region [17, 31]. We reexamined the Fat PCP pattern by visualizing endogenous Dachs. We segmented cells and calculated a nematic based on the anisotropy of Dachs perimeter intensity. Its angle reveals the axis and its length reveals the magnitude of anisotropy (Supplemental Experimental Procedures, Section 5, available online) [7, 17]. Locally averaged nematics reveal a Fat PCP pattern with strong polarity extending into the central wing pouch (Figures 1A–1C). Strikingly, Fat system polarity in this region corresponds to that of the Core PCP system, including pattern features near the DV and AP boundaries. Both Core and Fat PCP complexes have a clustered organization at cell contacts, but do not cocluster extensively (Figures S1A and S1B).

The Core PCP pattern is reorganized during wing morphogenesis [7]. We wondered whether the Fat PCP pattern changed as well, or whether opposing Fj and Ds gradients

would continue to guide its polarity. We therefore quantified Fat PCP nematics based on Ds::EGFP throughout pupal wing development. We also used clones expressing EGFP-tagged Dachs or Ds to quantify the vector direction of Fat PCP. We then compared the pattern of Fat PCP to that of the Core system (using Stbm::enhanced yellow fluorescent protein [EYFP]) and to expression gradients of Ds and Fj (Figures 1D–1L and S1F). Fat and Core PCP patterns change in parallel during prepupal morphogenesis—by 6 hAPF, they are organized in a fan-shaped pattern such that both Fz and Dachs domains orient toward the wing margin (data not shown). This pattern is stable until about 16 hAPF (Figures 1D, 1E, and S1C–S1E). The fan-shaped pattern assumed by Fat PCP is consistent with elevated Ds expression anterior to the AP boundary that becomes visible after pupariation (Figure 1F) [15, 32], while Fj expression remains high at the wing margin (Figure S1F) [27]. Thus, Fat PCP vectors at 16 hAPF point away from high levels of Ds near vein L3 toward high levels of Fj at the wing margin.

Fat PCP and Core PCP vectors diverge during pupal morphogenesis, starting shortly after 16 hAPF. At this time, anisotropic tissue flows reshape the wing blade, extending it along the PD axis and narrowing it along the AP axis. In vivo time-lapse imaging shows that the Core PCP pattern reorients to align with the PD axis of the wing (Figures 1D, 1G, 1J, and 1M–1O; Movie S1-1) [7]. Alignment of Core PCP with the PD axis is complete by 24 hAPF (Figure 1G), and the magnitude of PD polarity increases until 32 hAPF—roughly the time hairs form.

Fat system polarity behaves differently during tissue flows (Movie S1-2). While the Core PCP pattern reorients, the Fat PCP pattern maintains its alignment with Ds and Fj expression gradients (Figures 1E, 1H, 1K, and 1P–1R). Although Ds levels along the AP boundary decrease during tissue flows, its general pattern is not altered (Figures 1F, 1I, 1L, and S1F; Movie S1-3). Fat PCP is unchanged until 26 hAPF (hours after Core PCP has reoriented) (Movie S1-2), when the axis of the Fat PCP system shifts slightly to become even more orthogonal to the PD axis (Figure 1K). Thus, at the time of hair outgrowth, Fat PCP is oriented roughly orthogonal to Core PCP throughout much of the wing blade. They align only near the distal wing margin, and very close to the hinge. Here, Fat PCP nematics are small, but tend to orient along the PD axis (compare Figure 1J to Figure 1K).

Fat PCP vectors generally point toward the anterior wing margin anterior to L3 and posteriorly on the other side (Figures S1G, S1H, S2C, S2C′, and S2D–S2E‴; Movie S1-4). However, strikingly, wing veins (except L2) are associated with local disturbances in the direction of Fat PCP vectors, which flip over very short distances such that Ds and Dachs domains point toward veins from either side (Figures 1R, S1G, and S1I–S1L). Interestingly, this feature of the Fat PCP pattern does not correlate with opposing gradients of Ds or Fj (Figure S1F).

Fat and Core PCP Patterns Converge after Hairs Emerge

After wing hairs form, just before cuticle secretion, both Core PCP and Fat PCP patterns change again. The Fat polarity system undergoes a striking reorganization (Figures 2A–2C, 2K–2M, and S2). Anterior to vein L3, it rotates by 90° such that Dachs domains point toward the hinge; thus, Fat PCP has an identical axis, but opposite vector orientation, to Core PCP in this region (Figures S2D–S2F′; Movie S1-4). This reorientation is not guided by changes in Ds expression (Movie S1-3). Subsequently, posterior to L3, both PCP patterns rotate
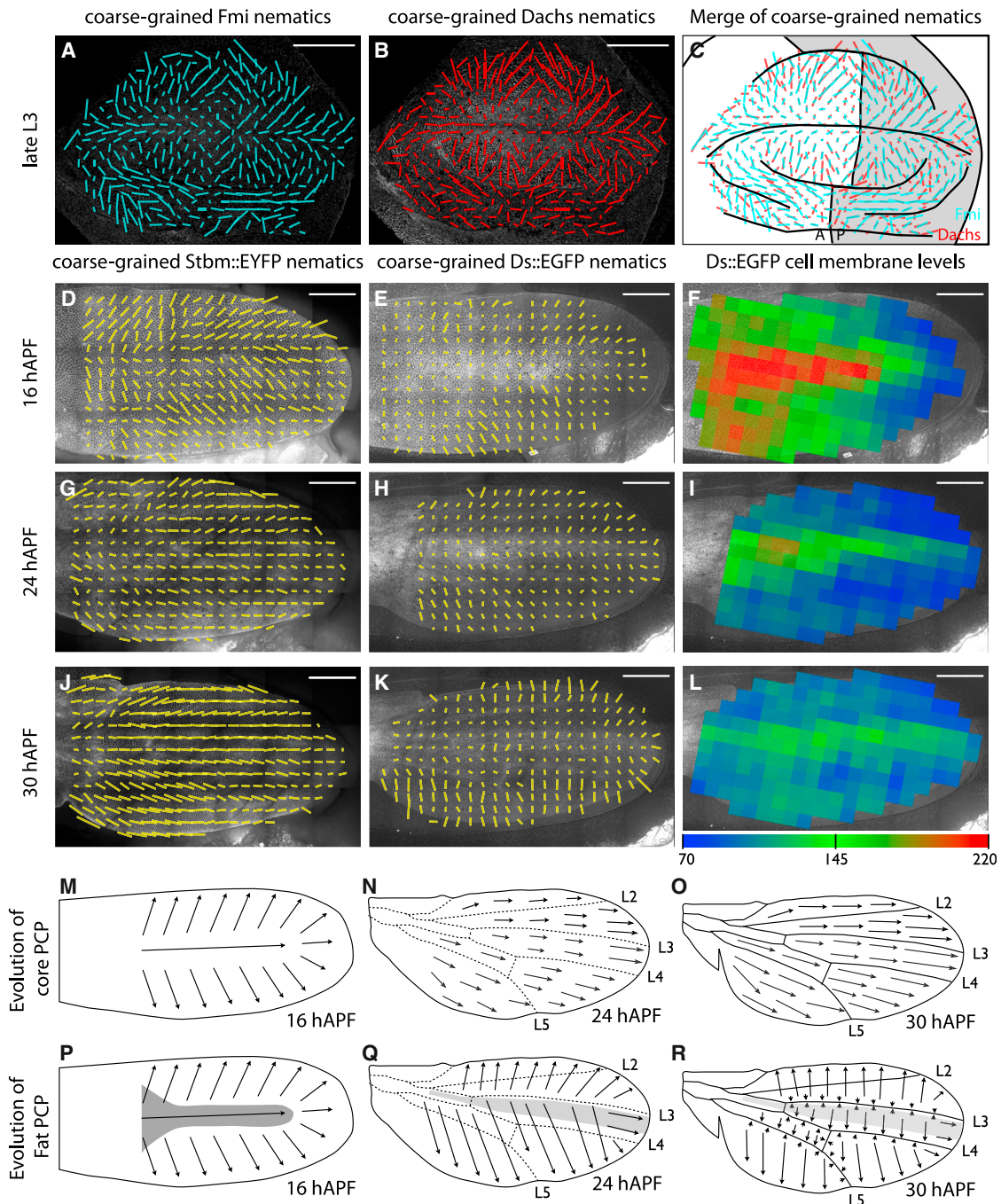
Figure 1. Evolution of Core PCP and Fat PCP during *Drosophila* Wing Development

(A–C) Coarse-grained Fmi (A) and Dachs (B) nematics quantified from the same wing disc and overlay of both patterns on a schematized wing disc (C).

(D–L) Stbm::EYFP (D, G, and J) and Ds::EGFP (E, H, and K) coarse-grained nematics and quantification of the Ds::EGFP gradient (F, I, and L) during pupal wing development at 16 (D–F), 24 (G–I), and 30 (J–L) hAPF. The average Ds::EGFP pixel intensity on cell interfaces shown in (F), (I), and (L) is encoded according to the colorbar in (L) (arbitrary units).

(M–O) Schematized Core PCP pattern during pupal wing development at 16 (M), 24 (N), and 30 (O) hAPF. Core PCP reorients from radial to PD polarity between 16 and 30 hAPF.

(P–R) Schematized Fat PCP pattern during pupal wing development at 16 (P), 24 (Q), and 30 (R) hAPF. Fat PCP reorients from radial to AP polarity between 16 and 30 hAPF.

Scale bars, 50 μm. See also Figure S1 and Movie S1.

by about 45° to align in opposite vector directions (Figures 2B, 2C, 2E, 2F, and 2I–2M; Movie S2). The resulting Fat and Core PCP pattern is remarkably similar to the pattern of cuticular ridges (Figures 2C, 2F, and 2H) [5]. In summary, identical patterns of Fat PCP and Core PCP emerge during the growth of the wing disc. The patterns remain aligned until the end of prepupal development. They diverge during tissue flows, when Core PCP orients distally, and then couple with opposite
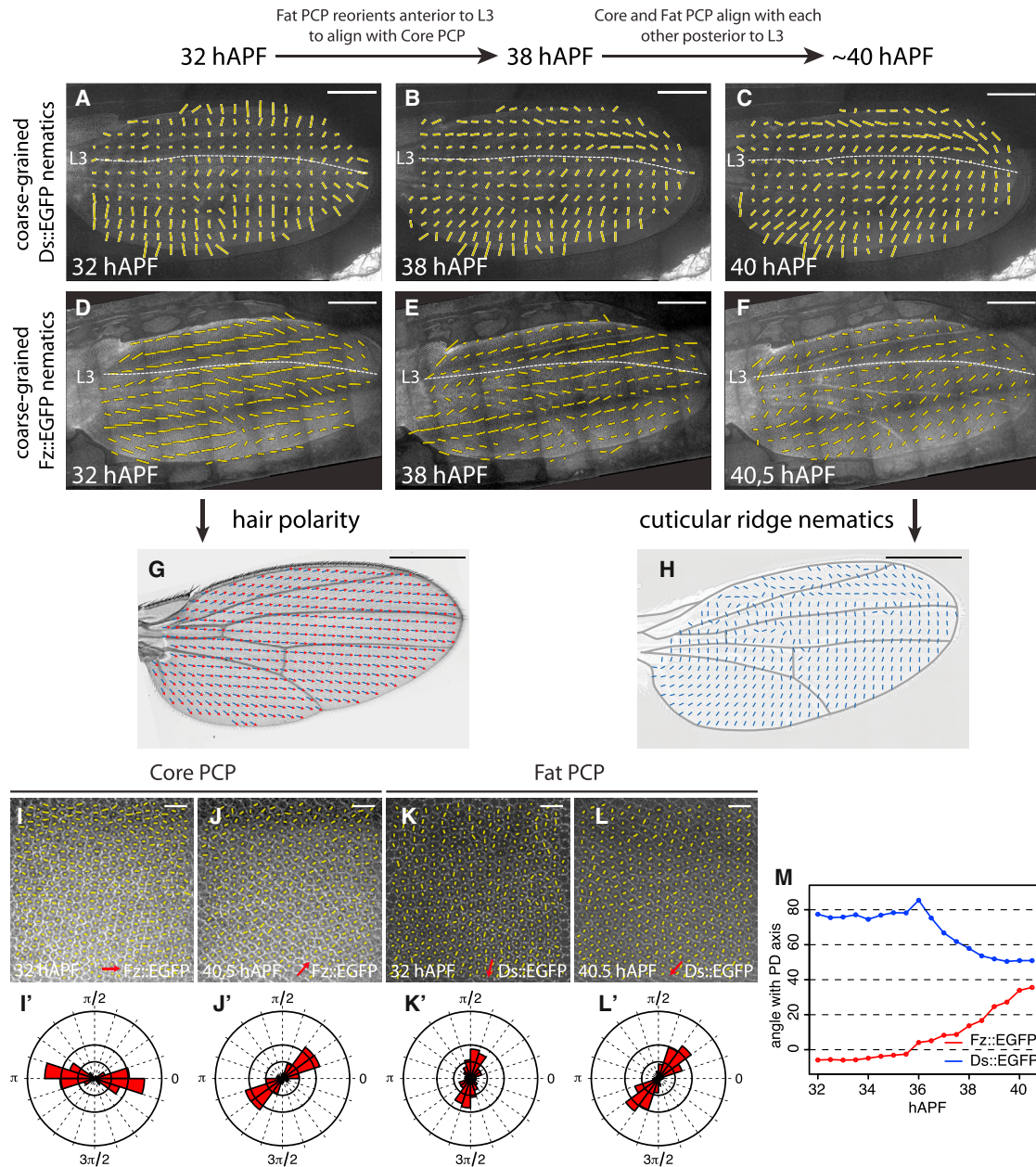
Figure 2. Core PCP and Fat PCP Systems Reorient after Hair Formation to Presage Cuticular Ridges

(A–C) Coarse-grained Ds::EGFP nematics at 32 (A), 38 (B), and 40 (C) hAPF. Nematics align with the PD axis anterior to L3 between 32 and 38 hAPF (A and B) and turn posterior to L3 between 38 and 40 hAPF.

(D–F) Coarse-grained Fz::EGFP nematics at 32 (D), 38 (E), and 40.5 (F) hAPF. Nematics anterior to L3 stay aligned with the PD axis, while those posterior to L3 turn between 38 and 40.5 hAPF.

(G and H) Coarse-grained hair polarity (G) and cuticular ridge nematics (H) were calculated according to Supplemental Experimental Procedures, Section 7. Note that ridge nematics are defined to be orthogonal to cuticular ridges to highlight alignment with Core and Fat PCP nematics.

(I–L) Single-cell nematics of Fz::EGFP (I and J) and Ds::EGFP (K and L) posterior to the L4 vein at 32 hAPF (I and K) and 40.5 hAPF (J and L).

(I′–L′) Rose diagrams displaying the orientation of single cell nematics in (I)–(L). Circles from inside to outside indicate 12.5%, 25%, and 50% of cells. Bin size is 18°.

(M) Quantification of changing angles between the averaged nematic and the PD axis for Fz::EGFP (red) and Ds::EGFP (blue) over time for the region shown in (I)–(L). Note that Fz::EGFP nematics turn counterclockwise and Ds::EGFP nematics turn clockwise. Thus, at 40.5 hAPF, Fz::EGFP and Ds::EGFP orient to opposite sides of the cell.

Scale bars, 50 μm (A–F) and 500 μm (G and H); 10 μm (I–L). See also Figure S2 and Movie S2.

vector directions (similar to their deduced relationship in the eye and anterior abdomen [9, 26–28]) to form a new pattern that presages cuticular ridges.

Several conclusions can be drawn from these observations. First, the Fat system cannot directly bias the PD orientation of Core PCP in pupal wings, because Core PCP reorients during flows, while Fat PCP is unchanged. Second, unlike Core PCP, patterns of Fat PCP are not influenced by tissue flows: gradients of Ds and Fj may be stronger orienting cues. Third, although the Fat PCP system clearly orients along expression
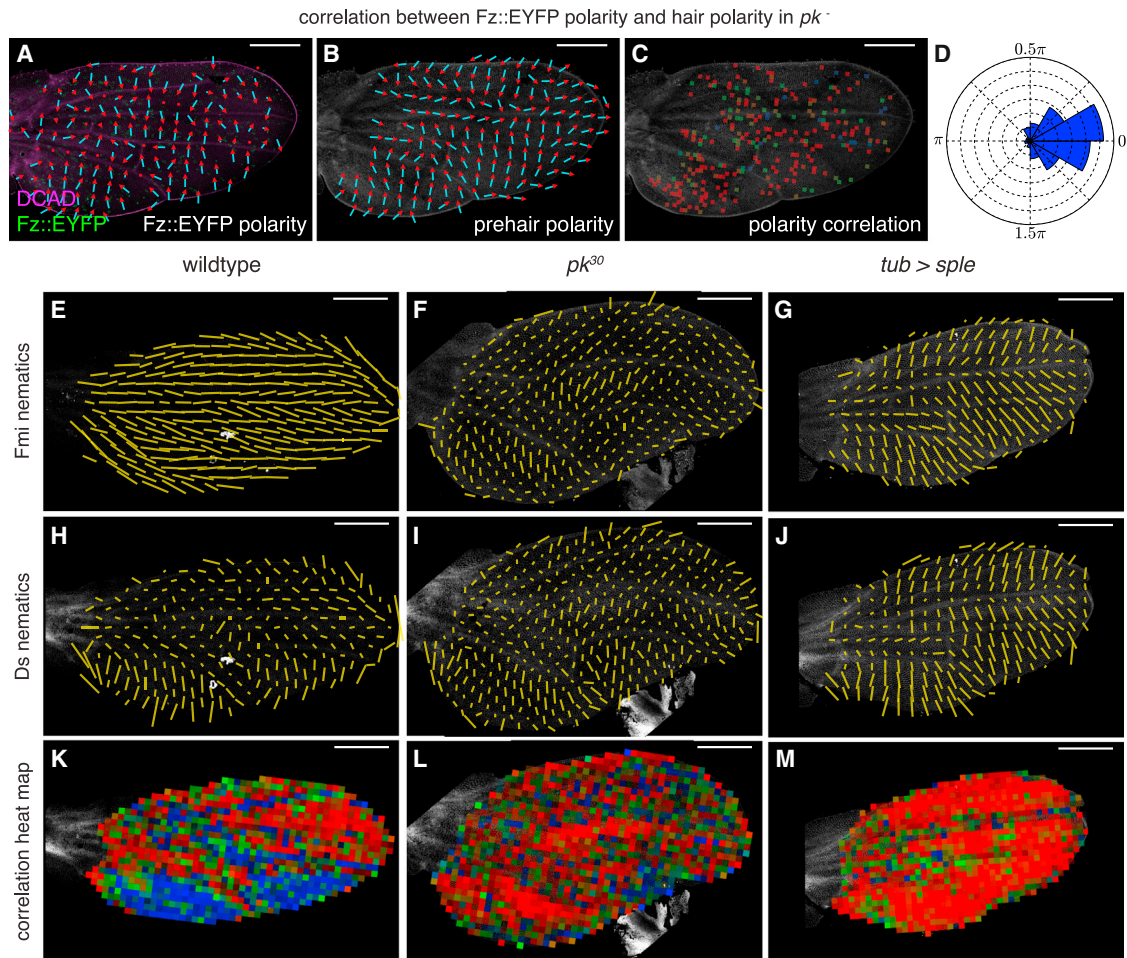
correlation between Fz::EYFP polarity and hair polarity in *pk* -

Figure 3. The Balance between Pk and Sple Controls the Amount of Coupling between PCP Systems

(A–D) Coarse-grained vector direction of Fz::EYFP clones (A; n = 395 clones) and prehair polarity (B) in a *pk¹/pk³⁰* pupal wing at 32 hAPF. (C) Position of individual Fz::EYFP clones and their correlation with prehair polarity. Red indicates parallel and blue antiparallel alignment of both vectors. (D) Distribution of angle differences between Fz::EYFP clone polarity and prehair polarity. Concentric circles from inside to outside indicate 5%, 10%, 15%, 20%, 25%, and 30% of clones. Bin size is 30°.

(E–J) Coarse-grained Fmi (E–G) or Ds (H–J) nematics in wild-type (E and H), *pk³⁰* (F and I), and *tub>sple* (G and J) pupal wings at 32 hAPF.

(K–M) Comparison between Fmi and Ds nematics in wild-type (K), *pk³⁰* (L), and *tub>sple* (M). The color of each box indicates the angular correlation between Fmi and Ds nematics (Supplemental Experimental Procedures, Section 8). Red indicates parallel and blue perpendicular alignment. Transparency of tiles encodes the combined local nematic order within both PCP systems. In opaque boxes, the nematic order of both PCP systems is high; within transparent boxes, the nematic order of at least one PCP system is low.

Scale bars, 50 μm. See also Figure S3.

gradients of Ds and Fj, it orients in response to other signals as well.

Sple Couples Core PCP to Fat PCP and Perturbs Distal Alignment in *pk* Mutants

What cues might regulate coupling and uncoupling of Fat and Core PCP? We noted that divergence of their patterns during tissue flows coincides with the time at which Pk is required for the establishment of normal hair polarity [33]. We wondered whether Pk might be required for divergence of Core and Fat PCP during tissue flows. Indeed, the hair polarity pattern in *pk* mutants resembles that of Fat PCP at the time hairs emerge: both are significantly orthogonal to the PD axis and reflect across L3 (Figures S2C, S2C′, and S4A; [15, 16]). To investigate this idea, we quantified and averaged Core PCP nematics in *pk⁻* pupal wings and compared them to the orientation of Ds nematics in the same wings (Figures 3F, 3I, 3L, and

S3F). While Fmi-based nematics are reduced in magnitude in *pk* mutants, these experiments reveal residual polarity of the Core PCP system that is different from the wild-type pattern and similar to that of Fat PCP (Figures 3E, 3F, 3H, 3I, 3K, 3L, and S3F). Thus, loss of the Pk isoform allows the Fat system to influence the Core PCP pattern during tissue flows when these systems normally diverge. To investigate the relationship between altered Core PCP and altered hair polarity, we compared the orientation of prehair emergence to Core PCP nematics (Figures S3A–S3D) and vectors (Figures 3A–3D). Hairs emerge toward Fz-containing domains in *pk* mutant wings, just as they do in wild-type, suggesting that Core PCP still controls hair orientation.

The Pk and Sple isoforms produced from the *pk-sple* locus differ in their N-terminal domains, are required in different tissues, and act antagonistically. Genetic analysis suggests that unopposed Sple activity alters the hair polarity pattern in
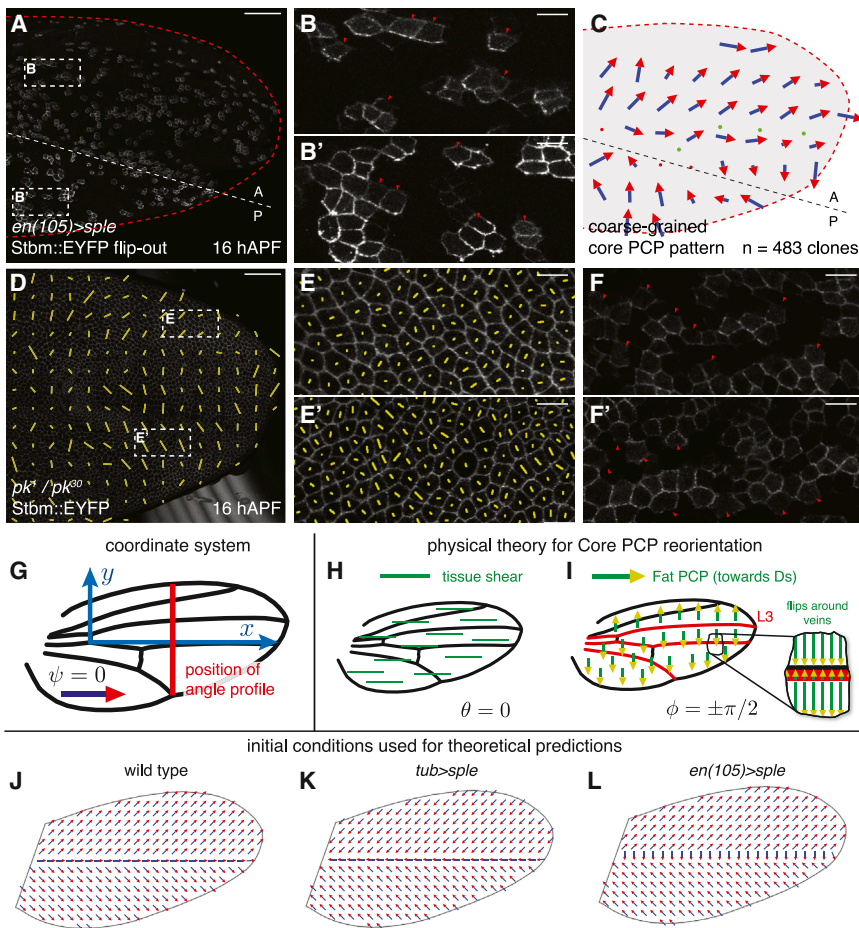
Figure 4. Sple Overexpression, but Not Loss, of Pk Reverses the Early Polarity Pattern

(A) Stbm::EYFP-expressing clones in a wing overexpressing *sple* in the posterior compartment (*en(105)>sple*) at 16 hAPF. Positions of the AP boundary and wing margin are indicated by white and red dashed lines, respectively.

(B and B′) Higher magnification views of the boxed regions shown in (A). Polarity of Stbm::EYFP is indicated by red arrowheads and is reversed in the posterior compartment.

(C) Coarse-grained global Core PCP pattern in *en(105)>sple* pupal wings at 16 hAPF, obtained by averaging information from 483 Stbm::EYFP-expressing clones from six pupal wings as described in [17]. Dashed lines indicate the wing margin and AP compartment boundary, green dots the position of the sensory organs along L3 and at the anterior crossvein.

(D) Coarse-grained Core PCP nematics quantified from Stbm::EYFP localization in a *pk¹/pk³⁰* pupal wing at 16 hAPF.

(E and E′) Higher magnification views of the boxed regions shown in (D) showing PCP nematics in single cells.

(F and F′) Stbm::EYFP clones in *pk¹/pk³⁰* pupal wing at 16 hAPF, located in similar regions as (B and B′). Stbm::EYFP polarity (red arrowheads) is similar to wild-type.

(G) Coordinate system based on vein positions. The origin is at the intersection of L4 with the ACV. The x axis goes through the distal end of L4, and the y axis is perpendicular to the x axis. Angles are defined to be zero whenever they point in positive *x* direction. Angles increase in counterclockwise direction.

(H and I) Physical theory describing the reorientation of Core PCP (Supplemental Theoretical Procedures, Section 1). Core PCP is coupled to a shear field oriented along the PD axis (H). Also, there is a coupling to a simplified Fat PCP direction field ϕ (I) that is everywhere parallel to the AP axis. The direction of the ϕ pattern flips at vein L3 and around the veins L3, L4, and L5.

(J–L) Simplified initial conditions used for numerical solutions of Equation 1.

See also Figure S4.

pk mutant wings [16], and genetic experiments suggest that Sple may sensitize Core PCP to the Fat system [15, 18, 19]. To ask whether Sple might promote alignment of Fat and Core PCP domains, we overexpressed Sple throughout the wing using *tubulin*-Gal4 (*tub>sple*). Quantifying Core and Fat PCP nematics at 32 hAPF (Figures 3G, 3J, 3M, and S3G) reveals striking alignment between the axes of Core and Fat PCP (Figure 3M). In most regions, the Core PCP pattern remains correlated with that of Fat PCP and does not reorient distally. Regions near veins—particularly L3—are exceptions. Here, the direction of Fat PCP vectors flips over short distances (Figures S1I and S1L), while the orientation of wing hairs suggests that Core PCP bends smoothly. In general, the altered Core PCP pattern presages the changed hair polarity pattern in adult *tub>sple* wings (Figure S4B). These data show that Sple promotes coupling of Core and Fat PCP domains.

The orientation of hairs in Sple-overexpressing wings suggests that Fz domains point toward L3 and somewhat proximally. This would indicate that Fz is on opposite boundaries from Dachs and Ds, exactly the reverse orientation to that observed in the larval wing disc (Figure S4B). To confirm this, we quantified the polarity of Fz::EYFP- and EGFP::Pk-expressing clones in 32 hAPF pupal wings overexpressing Sple in the posterior compartment (Figures S3H–S3K). Indeed,

Fz::EYFP localizes to anterior and proximal cell boundaries and EGFP::Pk to posterior and distal cell boundaries in the overexpression region (Figures S3J and S3K). Thus, Sple promotes coupling of the Core and Fat PCP systems with opposite polarities, and this coupling inhibits reorientation of Core PCP during tissue flows. Unopposed Sple activity in *pk* mutants likely perturbs Core PCP orientation by this mechanism. Consistent with this idea, reducing Fat PCP activity suppresses hair polarity defects in *pk* mutants [15], and in wings overexpressing Sple (Figures S3L–S3Q).

The altered hair polarity patterns caused by *pk* mutation and continuous Sple overexpression are not identical (Figures S4A, S4B, and S4D). Although both perturbations tend to deflect hair polarity orthogonal to the PD axis and toward vein L3, the remaining PD component is proximal in Sple-overexpressing wings, but distal in *pk* mutant wings. Much more similar hair patterns are produced when Sple expression is limited to pupal stages (Figures S4A–S4F) [5]. This suggests that larval and prepupal Sple overexpression, but not *pk* mutation, reverses the vector direction of the early, fan-shaped Core PCP pattern. Indeed, analyzing Stbm::EYFP and EGFP::Pk clones shows the orientation of Core PCP is reversed by Sple overexpression in larval discs and 16 hAPF wings, but is normal in *pk* mutants (Figures 4A–4F′ and S4G–S4I′).

Single-molecule fluorescence in situ hybridization (smFISH) suggests that wing discs and 6 hAPF wings express smaller amounts of Sple than 18–36 hAPF wings (Figures S4J–S4N). It may be that low amounts of Sple are insufficient to reverse polarity in the presence of other orienting signals in the wing disc [17].

The Core PCP and Fat PCP patterns in Sple-overexpressing wings are similar but not identical, particularly near veins. Other factors are needed to explain the observed Core PCP and wing hair patterns quantitatively. These may include tissue shear and the tendency of Core PCP domains to align locally. The interplay of such effects can be quantitatively investigated by a physical theory for Core PCP orientation dynamics.

Quantitative Study of Sple-Dependent Coupling of Core and Fat PCP using a Physical Model

Previously, we used a hydrodynamic description to show that Core PCP reorientation in wild-type pupal wings can be quantitatively explained by a coupling to local tissue shear and rotation [7]. By tissue shear, we mean tissue deformation similar to convergence-extension where the axis of extension defines the shear axis. Shear is caused by cell elongation, cell divisions, and cell rearrangements, which are oriented along the PD axis in the pupal wing. Here, we extend this hydrodynamic model to explore the effects of an additional Sple-mediated coupling of Core PCP to Fat PCP during tissue flows. The hydrodynamic approach describes the dynamic behavior of cell polarity on tissue scales by continuous variables. We denote the local angle of Core PCP (pointing toward Fz) with respect to the PD axis by ψ (Figure 4G). Similarly, we introduce the angle ϕ of Fat PCP (pointing toward Ds) and the angle θ describing the local axis of tissue shear (Figures 4H and 4I). We focused on dynamics of the Core PCP direction field ψ. Starting from simplified initial conditions corresponding to wild-type and mutant Core PCP patterns observed at 16 hAPF (Figures 4J–4L), we solved an equation for the time evolution of the Core PCP direction ψ that is of the form

$$\frac{\partial \psi}{\partial t} = k\nu \sin(2[\psi - \theta]) - \zeta \sin(\psi - \phi) + \kappa \Delta \psi, \qquad \text{(Equation 1)}$$

where the symbol k denotes the local rate of shear along the axis given by θ, and the coefficient ν denotes the strength of shear coupling. If ν is negative (positive), Core PCP tends to align parallel (perpendicular) to the shear axis. Here, we treat the product $k\nu$ as a single independent parameter. The coupling of Core PCP to Fat PCP is described by the coefficient ζ. For negative ζ, Core PCP (pointing toward Fz) tends to align in the opposite direction as Fat PCP (pointing toward Ds). For positive ζ, Core PCP tends to align in the same direction as Fat PCP. The tendency of Core PCP vectors to locally align with each other is captured by an interaction with strength κ, which is always positive. The symbol Δ denotes the Laplace operator. At points where the value of ψ attains a local maximum (minimum), $\Delta \psi$ is negative (positive). In Equation 1, we have ignored advection and local tissue rotation for simplicity.

In order to capture the possible effects of Sple overexpression on Core PCP reorientation, we characterized tissue overexpressing Sple by different values of the parameters $k\nu$, ζ, and κ. For wild-type tissue, we denote these parameter values by $k\nu_{wt}$, ζ_{wt}, and κ_{wt} and for tissue overexpressing Sple by $k\nu_{so}$, ζ_{so}, and κ_{so}. This reflects the possibility that Sple overexpression could change any of these parameters. Long-term time-lapse imaging of Sple-overexpressing wings shows roughly normal tissue flow and shear (Figures S4O and S4P; Movie S3), so differences between the value of $k\nu_{so}$ and $k\nu_{wt}$ should only reflect changes in the response to tissue shear. Using our model, we can test which parameter changes are necessary to account for our observations.

In order to numerically solve Equation 1, we considered a simple homogeneous shear pattern oriented along the PD axis $(\theta = 0)$ (Figure 4H). Similarly, we used a simplified unchanging Fat PCP pattern oriented perpendicular to the PD axis everywhere $(\phi = \pm \pi/2)$. Anterior to the L3 vein, Ds points anteriorly $(\phi = +\pi/2)$ and posterior to this vein, Ds points posteriorly $(\phi = -\pi/2)$ (Figure 4I). In addition, we introduce flips around veins L3, L4, and L5 (Supplemental Theoretical Procedures, Section 4). We also imposed boundary conditions involving an elastic element coupling margin bristle direction and Core PCP at the margin (Supplemental Theoretical Procedures, Section 2). These were motivated by observed hair and bristle patterns. Thus, our model predicts not only the orientation of wing hairs but also the orientation of wing margin bristles (Figure S5P).

A Single Parameter Set Accounts for Hair Polarity Patterns in Wild-Type and Sple-Overexpressing Wings

Interestingly, expressing Sple ubiquitously at different stages of wing development causes distinct hair polarity patterns (Figures 5A, 5D, 5G, and 5J). In addition, limiting Sple overexpression to the posterior compartment causes reproducible bending of the hair polarity pattern near the AP boundary (Figures 5M, 5P, and 5S). We aimed to find one set of parameters ($k\nu_{wt}$, ζ_{wt}, κ_{wt}, $k\nu_{so}$, ζ_{so}, and κ_{so}) that can account for all of these hair polarity patterns. Conditions studied were as follows: (1) wild-type; (2) early ubiquitous Sple overexpression (during larval and prepupal stages); (3) late ubiquitous Sple overexpression (starting at pupal stages); (4) permanent ubiquitous Sple overexpression; and (5) early, (6) late, and (7) permanent Sple overexpression in the posterior compartment. For wild-type and for late Sple overexpression (conditions 1, 3, and 6), we started from wild-type initial conditions (Figure 4J) corresponding to the fan-shaped Core PCP pattern at 16 hAPF. For early and permanent posterior Sple overexpression (conditions 5 and 7), we started from a fan-shaped pattern that is inverted only in the posterior compartment (Figure 4L), consistent with Figures 4A–4C. Similarly, for early and permanent ubiquitous Sple overexpression (conditions 2 and 4), we started from a completely inverted fan-shaped pattern (Figure 4K). Starting from these initial conditions, we explored parameter space and did indeed find a single parameter set, shown in Table S2 (model A), for which our model produces the key features of wild-type and all genetically perturbed wing hair patterns (Figure 5; Movies S4-1, S4-2, S4-3, S4-4, S4-5, S4-6, and S4-7). To facilitate a quantitative comparison, we plotted the angles of the calculated final Core PCP direction (red solid lines) together with the observed wing hair direction field (blue solid lines) as a function of the distance from vein L4 (along the line shown in red in Figure 4G; Supplemental Experimental Procedures, Section 9) in Figures 5C, 5F, 5I, 5L, 5O, 5R, and 5U.

The parameter values were determined as follows (Supplemental Theoretical Procedures, Sections 3 and 5; Table S2). In all genetically perturbed conditions (2–7), wing hair angles turn over characteristic distances, denoted by λ_{wt} and μ_{so}. These turning distances are related to the strength with which Core PCP vectors tend to align with each other, compared to

experiment: adult wing hair pattern

theory: predicted Core PCP pattern at wing hair outgrowth

angle profile: comparison of experiment and theory

(1) wild type

(2) early *tub>sple*

(3) late *tub>sple*

(4) permanent *tub>sple*

(5) early *en(105)>sple*

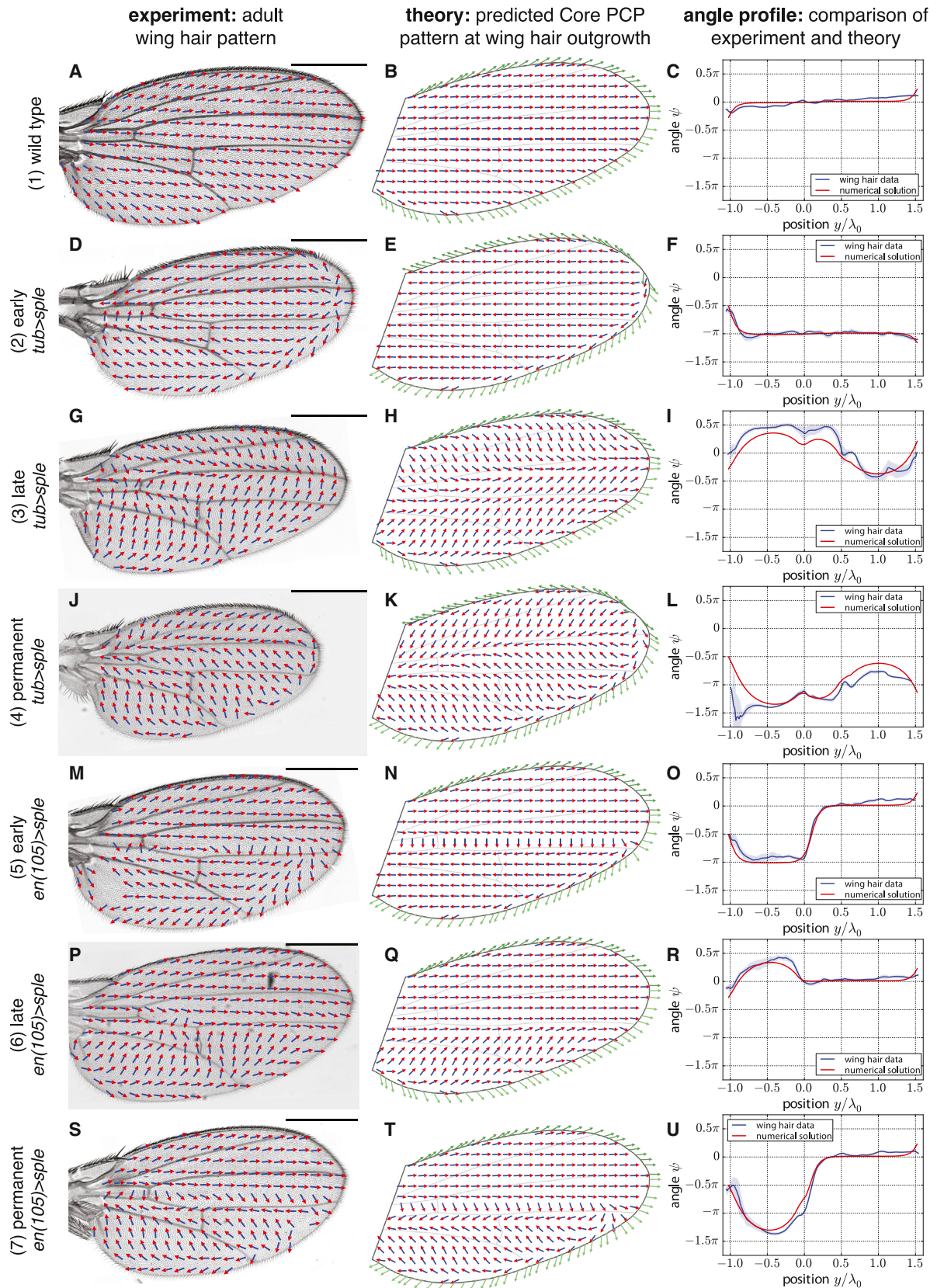(6) late *en(105)>sple*

(7) permanent *en(105)>sple*

Figure 5. Qualitative and Quantitative Prediction of Hair Polarity Patterns in Different Sple Overexpression Conditions

Results of our physical theory for all seven conditions of space- and time-dependent Sple overexpression. Parameters used are listed in Table S2 (model A). Quantified wing hair patterns (A, D, G, J, M, P, and S) are compared to numerical solutions of Equation 1 at the time of wing hair outgrowth (B, E, H, K, N, Q,

(legend continued on next page)

their tendency to align with shear ($\lambda_{wt} = (\kappa_{wt}/2|kv_{wt}|)^{1/2}$) or with Fat PCP ($\mu_{so} = (\kappa_{so}/\zeta_{so})^{1/2}$). To reduce the space of possible parameter values, we compared the linear profiles of observed wing hair angles to stationary solutions of Equation 1. This allows us to directly measure λ_{wt} and μ_{so} using a fit of the theoretical profile to the experimental data (Table S1).

From earlier work [7], we know that Core PCP reorientation during pupal stages in wild-type can be accounted for without input from an AP-oriented signal like that of Fat PCP. Therefore, we set $\zeta_{wt} = 0$, corresponding to no coupling to Fat PCP. With this assumption, a value for kv_{wt} can be obtained from the data by fitting the dynamic solution of Equation 1 to the observed time-dependent Stbm::EYFP pattern in the whole wing (Figures 1D, 1G, and 1J; Movie S4-8; Supplemental Theoretical Procedures, Section 5). The best fit was obtained for $kv_{wt} = -0.1 h^{-1}$. From the values of λ_{wt} and kv_{wt} follows the value of the neighbor coupling κ_{wt} (Tables S1 and S2).

For tissue overexpressing Sple, we cannot quantify the full dynamics of Core PCP reorientation. Therefore, we compared the final state of the dynamic solutions of Equation 1 to the quantified wing hair patterns. We found that we could only account for all observed hair patterns by introducing an anti-parallel coupling to Fat PCP ($\zeta_{so} < 0$; model A). Furthermore, the magnitude $|\zeta_{so}|$ must be at least two to three times larger than $|kv_{so}|$, suggesting that under Sple overexpression conditions, coupling to Fat PCP dominates over coupling to shear. Because of this, we cannot determine the precise value of the shear coupling in Sple overexpression conditions kv_{so}. Thus, for model A, we chose $kv_{so} = kv_{wt}$. Note that models that alter the axial response to flow but do not include vectorial Sple-dependent coupling fail to reproduce some of the experimentally observed wing hair pattern (model B; Figures S5A–S5L; Supplemental Theoretical Procedures, Section 6).

Thus, for the first time, we can quantitatively explain the patterns of hair polarity observed in a set of genetic perturbations. Core polarity defects caused by Sple overexpression at different times can be explained by taking into account just three physical mechanisms (captured by three parameters) that act on the initial fan-shaped Core PCP pattern: (1) coupling to tissue shear, (2) Sple-dependent vector coupling to Fat PCP, and (3) the tendency of Core PCP to align locally. When Sple is overexpressed only during tissue flows, the initially normal Core PCP pattern does not properly reorient along the PD axis because Sple-dependent coupling to Fat PCP is stronger than the effects of tissue shear. However, coupling of Core to Fat PCP does not result in a perfectly AP hair polarity pattern (like that of Fat PCP) because of the third parameter: the tendency of Core PCP domains to locally align. This disfavors discontinuities in Core PCP vector orientation and causes these vectors to bend smoothly as they approach L3. This model also provides a theoretical explanation for the altered pattern of hair polarity in pk mutants, which is produced by mechanisms that are mimicked by late Sple overexpression (Figures S4A, S4C, and S4E). Our theory also accurately predicts the proximal-oriented hair polarity observed

when Sple overexpression is discontinued before the onset of tissue flows: here, tissue shear acts on the reversed initial pattern to align its axis proximodistally, but does not correct its vector direction (Figures 5D, 5E, 5M, and 5N). This clearly shows that the PD shear signal operating at pupal stages provides axial rather than vector information. This axial signal normally operates on the preexisting Core PCP pattern to produce distally oriented Core PCP.

Sple Couples Core and Fat PCP after Hair Formation to Produce the Pattern of Cuticular Ridges

After hairs form, Core and Fat PCP vectors become aligned in opposite directions and form a new pattern like that of ridges (Figures 2 and S2). Fat vectors rotate anterior to L3 to align with Core PCP along the PD axis. Posterior to L3, Fat and Core PCP vectors both adjust their polarity to achieve a compromise orientation. To investigate how the Core and Fat PCP systems influenced each other during this process, we quantified Fat and Core PCP nematics at 40 hAPF in $stbm^6$ and ft^1 mutant wings, respectively (Figures 6G and 6M). ft^1 is a hypomorphic mutant with altered wing shape but normal hair polarity [15]. Although loss of Stbm does not affect Fat PCP at earlier stages (Figure S6C), it blocks reorientation of Fat PCP after hair formation such that it remains oriented along the AP axis throughout the wing (Figures 6D, 6M, 6P, 6P′, 6S, and 6S′). In contrast, loss of Fat only affects the late Core PCP pattern posteriorly—consistent with posterior-specific ridge defects in these wings (Figures 6C, 6G, 6J, and 6J′) [15]. This suggests that Core PCP determines the orientation of Fat PCP vectors anteriorly but that both influence each other posteriorly.

Since Sple promotes coupling of Fat and Core PCP vectors with opposite polarities, we investigated whether changes in the balance between Pk and Sple might occur at this time. Indeed, in vivo time-lapse imaging of endogenous EGFP-tagged Pk reveals that Pk levels decrease starting at 35 hAPF (Movie S5-1). In contrast, smFISH shows that Sple expression persists (Figure S4N). We had noted that loss of Sple did not affect the Core PCP pattern in early pupal wings (Figures S6A and S6B). To ask whether Sple was required later to reorganize Core and Fat PCP patterns after hair formation, we quantified these patterns in sple mutant wings. Indeed, removing Sple prevents the antiparallel alignment of Core and Fat PCP vectors posterior to L3 (Figures 6B, 6F, 6I, 6I′, 6L, 6R, and 6R′). Surprisingly, Fat PCP still reorients to point along the PD axis anterior to L3 (Figures 6L, 6O, and 6O′). Thus, Sple is only essential for coupling posterior to L3—consistent with the posterior-specific ridge defects seen in sple mutant wings [5]. Anteriorly, Fat PCP can obey orienting signals from Core PCP independently of Sple. Loss of Pk alone may allow weak antiparallel coupling between the two systems.

In pk mutants, Core PCP vectors point along the AP axis when hairs form (Figures 3A and 3F). Although Pk levels drop by the time cuticle is secreted, pk mutants develop abnormally oriented cuticular ridges [5]. Thus, we wondered whether the abnormal Core PCP pattern at the time of hair formation disturbed the subsequent reorganization of Fat PCP to form

and T). In the numerical solutions of Equation 1, bulk polarity (blue and red arrows) as well as the direction of wing margin bristles (green arrows) are indicated (see Supplemental Theoretical Procedures, Section 2). (C, F, I, L, O, R, and U) Direct comparison of experimental (blue solid lines) and theoretical (red solid lines) polarity patterns. We plot angles for both along the line shown in red in Figure 4G. For the experimental curves, we quantified hair polarity in at least eight wings for each condition. The blue-hatched region indicates the circular SD of quantified wing hair angles (Supplemental Experimental Procedures, Section 9). The theoretical curves correspond to the respective polarity patterns shown in (B), (E), (H), (K), (N), (Q), and (T).

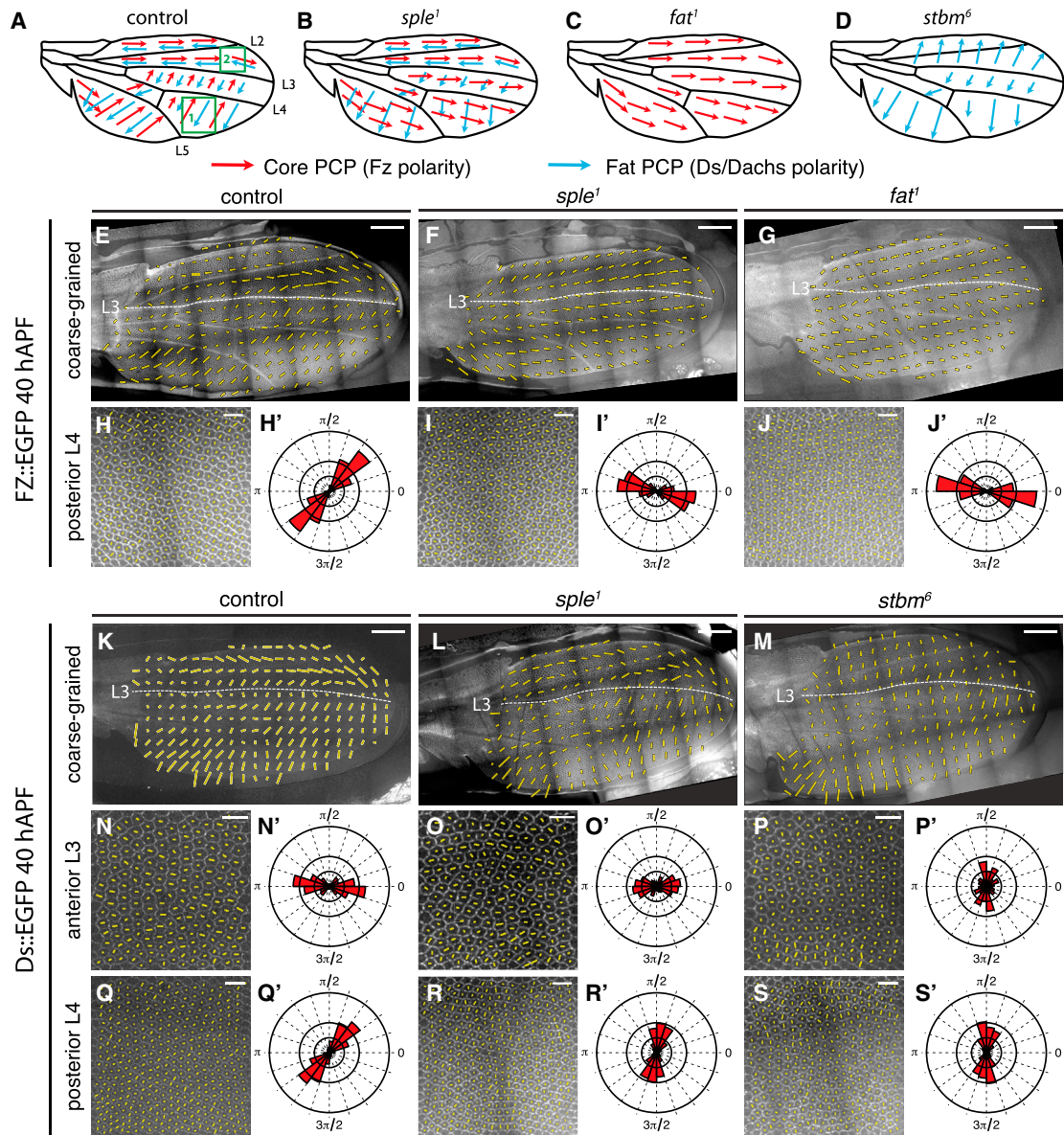Scale bars, 500 μm (A, D, G, J, M, P, and S). See also Figure S5 and Movie S4.

Figure 6. Activity of Both PCP Systems Is Required for Their Realignment after Hair Formation

(A–D) Schemes indicating orientations of Core and Fat PCP systems in wild-type (A), *sple¹* (B), *ft¹* (C), and *stbm⁶* (D) pupal wings at 40 hAPF.

(E–G) Coarse-grained Fz::EGFP nematics in control (E), *sple¹* (F), and *ft¹* (G) pupal wings at 40 hAPF.

(H–J′) Fz::EGFP staining and single-cell nematics (H–J), and rose diagrams quantifying the respective nematic orientations (H′–J′) in region 1 (green box in A) in the same wings as (E)–(G).

(K–M) Coarse-grained Ds::EGFP nematics in control (K), *sple¹* (L), and *stbm⁶* (M) pupal wings at 40 hAPF.

(N–S′) Ds::EGFP staining and single-cell nematics in boxed regions 2 (N–P) and 1 (Q–S), and rose diagrams quantifying the respective nematic orientations (N′–S′) the in the same wings as (K–M).

Scale bars, 50 μm (E–G and K–M) and 10 μm (H–J and N–S). In rose diagrams, circles from inside to outside indicate 12.5%, 25%, and 50% of cells. Bin size is 18°. See also Figure S6.

the ridge pattern. Indeed, Fat PCP no longer reorients along the PD axis in *pk* mutant wings: it remains aligned with Core PCP along the AP axis (Figures S6D–S6H′; Movie S5-2). Thus, evolution of the Core and Fat PCP ridge pattern depends on earlier Pk-dependent alignment of Core PCP with the PD axis.

Hair Polarity in *fz* and *stbm* Mutants Follows that of the Fat System

fz and *stbm* mutants, which lack all Core PCP function [33], have similar and reproducible hair polarity patterns different

from those of *pk* mutants [4, 34]. We noticed that these patterns are almost exactly antiparallel to those produced by continuous uniform Sple overexpression (Figures 7A–7C and 7F–7H), which couples Core PCP to the Fat system. Could Fat PCP guide hair polarity when Core PCP is absent? Indeed, comparing the orientation of emerging hairs and Ds nematics in *fz* and *stbm* mutant wings reveals strong correlation (Figures 7J–7Q and S7A–S7F′). Hairs grow toward Dachs-containing boundaries; the opposite orientation as in Sple-overexpressing wings (Figures 7G and 7H). Exceptions occur directly
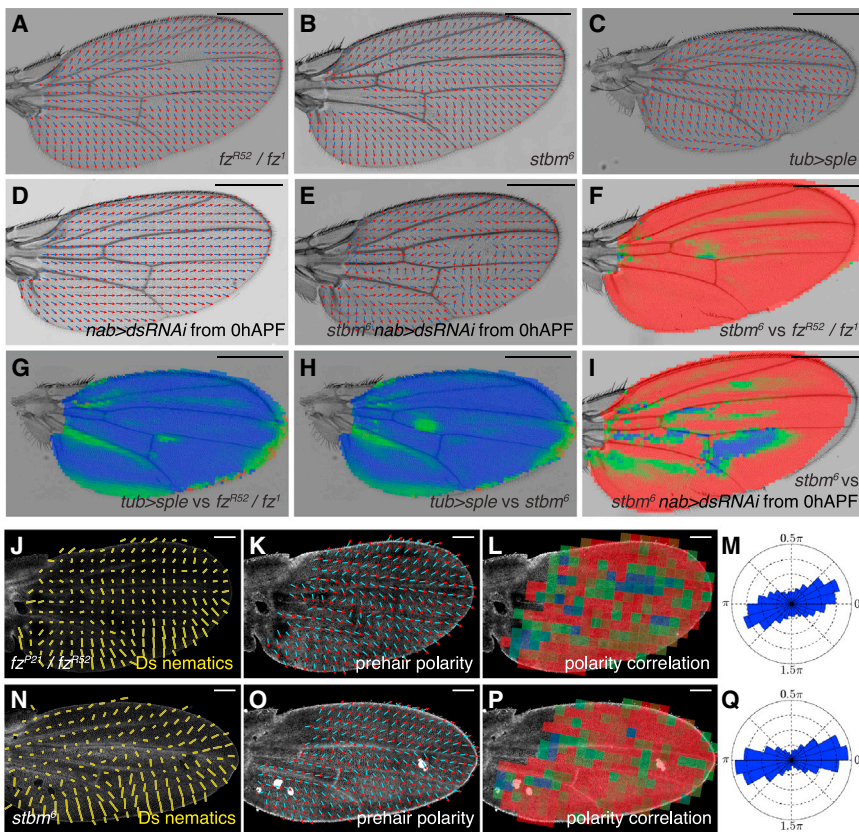
Figure 7. Perturbations of the Fat PCP System Influence the Hair Pattern in *fz* and *stbm* Mutants

(A–E) Quantification of hair polarity in fz^1/fz^{R52} (A), $stbm^6$ (B), *tub>sple* (C), *nab>ds*-RNAi from 0 hAPF (D), and $stbm^6$ *nab>ds*-RNAi from 0 hAPF (E) adult wings.

(F–I) Quantitative comparisons of averaged hair polarity patterns between fz^1/fz^{R52} and $stbm^6$ (F), fz^1/fz^{R52} and *tub>sple* (G), $stbm^6$ and *tub>sple* (H), and $stbm^6$ and $stbm^6$ *nab>ds*-RNAi from 0 hAPF (I). Red indicates parallel alignment of hair polarities, and blue indicates antiparallel hair polarities.

(J–Q) Coarse-grained Ds nematics (J and N) correlate with the orientation of prehairs (K and O) in fz^{P21}/fz^{R52} (J–M) and $stbm^6$ (N–Q) pupal wings at 35 hAPF. (L and P) Quantitative comparison between coarse-grained Ds nematics and prehair polarities in (J and N) and (K and O), respectively. Red indicates parallel and blue perpendicular alignment between Ds nematics and prehairs. (M and Q) Rose diagram indicating the distribution of angles between Ds nematics and hair polarities in the wings shown in (J and K) and (N and O), respectively.

Scale bars, 500 μm (A–I) and 50 μm (J–L and N–P).

See also Figure S7.

Discussion

The relationship between the Core and Fat PCP systems has been a vexed issue. Some argue that Fat PCP provides global cues to direct the pattern of Core PCP, which then orients structures such as hairs and bristles [26, 36]. Others have suggested that these systems contribute independently to morphological polarization [21, 22]. We resolve this problem by showing that the balance of Pk and Sple activities regulates coupling between Core and Fat PCP. Pk allows uncoupling, whereas Sple links the two systems with opposite vector orientation (i.e., Fz and Ds are on opposite cell boundaries). In the wing, Pk is needed to uncouple Core and Fat PCP during tissue flows. This allows Core PCP to reorient distally and guide hair formation, while the Fat system stays oriented along the AP axis. When Pk is lost and Sple dominates, the systems are coupled during flow and Core PCP is misoriented. Later, Sple is required to couple the two systems and generate the cuticular ridge pattern. It has been proposed based on genetic observations that Sple allows the Core PCP system to respond to cues from Fat PCP [15, 18, 19]; our findings provide concrete molecular support for this idea. They further suggest that when Core and Fat PCP are coupled, either partner can determine the orientation of their joint pattern: Core PCP guides Fat PCP to form the cuticular ridge pattern.

Although Fat and Core PCP vectors can uncouple when Pk is present, they are aligned in the wing disc, despite the presence of Pk. Here, they point in the same direction—unlike when Sple dominates. This may suggest that Core and Fat PCP have a weak tendency to align when Pk is present, but that this can be overcome later by tissue flows. This may explain why Fat PCP is needed for some aspects of the larval Core PCP pattern near the hinge [12, 17]. Alternatively, Fat PCP may influence Core PCP through effects on growth orientation [2, 7].

adjacent to the L3 and L4 veins (Figures S7I and S7J). Thus, while Fat PCP generally guides hair outgrowth in *fz* and *stbm* mutants, other mechanisms favoring local hair alignment dominate when Fat PCP vectors change over short distances (as they do near veins).

To ask whether these mutant hair polarity patterns depend on Fat PCP, we knocked down *ds* in a $stbm^6$ background starting at pupariation. In an otherwise wild-type background, late *ds* knockdown does not perturb hair polarity (Figure 7D). In contrast, *ds* knockdown in $stbm^6$ mutants alters the hair pattern (Figures 7B, 7E, and 7I). Furthermore, a new feature emerges in these wings: hairs tend to point toward and flip across longitudinal veins 3–5 and both crossveins (Figures S7G–S7J′). Thus, many aspects of the hair polarity pattern in $stbm^6$ mutants depend directly on the Fat PCP system. Loss of both systems uncovers orienting signals associated with wing veins.

Notably, hair polarity is still locally aligned when both Ds and Stbm are absent (Figure 7E), extending previous observations [35]. To further investigate this, we induced ft^8 null mutant clones in $fzP21/fzR^{52}$ mutant wings (Figures S7K–S7P). Cells lacking *ft* in this background should have no information from either PCP system. Hair polarity still aligns between neighboring cells in *ft, fz* double-mutant tissue (Figures S7N–S7P), confirming that this coordination is independent of both PCP systems. In summary, when Core PCP and Fat PCP patterns differ, hairs follow Core PCP and orient toward Fz-containing domains. If Core PCP domains cannot polarize, then the Fat PCP pattern biases hair outgrowth such that hairs orient toward Dachs. In the absence of both systems, hairs still align locally and obey signals associated with wing veins.

Our findings highlight the hysteresis of Core PCP patterns, i.e., they depend not only on current input (such as tissue flows or changed balance between Pk and Sple) but also on the patterns that precede them. Early Sple overexpression is an illuminating example. Sple overexpression prior to tissue flows reverses the orientation of the early Core PCP pattern; in the absence of further Sple expression, this reversal is preserved as the Core PCP axis realigns with the PD axis in pupal wings, eventually reversing hair orientation. Thus, pupal reorienting signals act mainly on the axis, rather than the vector, of Core PCP. Axial information may be provided by oriented cell divisions and rearrangements. It may also be present in PD cell elongation and alignment of microtubules with the PD axis. However, an axial signal is inconsistent with vectorial input from signaling gradients, or with a requirement for polarized (as opposed to axially aligned) microtubules at this stage. The observed hysteresis of Core PCP patterns suggests that the disturbed orientation of Core PCP (and hairs) in *ft* mutant pupal wings could derive from the altered pattern in larval discs, as polarity defects propagate during pupal tissue flows. Our data are inconsistent with a direct role for Fat PCP in orienting Core PCP distally at pupal stages, because their patterns do not agree at this time.

Understanding hysteresis in PCP patterns also helps resolve the puzzle as to how they specify distinct orientations of hairs and ridges. Based on phenotypes caused by timed Sple overexpression, it was proposed that the ridge pattern posterior to L3 is specified by an early (pre-18 hAPF) Sple- and Fat-dependent signal oriented along the AP axis, while the pattern anterior to L3 depends on a later Pk-dependent signal oriented in the PD axis [5, 15]. It was unclear what cellular features posterior to L3 might persist through subsequent Core PCP reorganization to guide cuticle deposition many hours later (40 hAPF). Our findings confirm the general idea that Sple allows Fat PCP to influence Core PCP and ridge orientation [15, 19]. But we show that this occurs just before cuticle secretion, as loss of Pk allows Sple to couple Fat and Core PCP and generate the ridge pattern. Earlier Sple overexpression (like loss of Pk) affects ridges because the PD-oriented Core PCP pattern does not develop properly. This affects the subsequent evolution of the ridge pattern.

The reproducible hair polarity patterns characteristic of different Core PCP mutants have always been hard to explain. We present a physical model that accounts for all the hair polarity patterns in wild-type wings, and in wings overexpressing Sple at different times. We show that these patterns can be quantitatively understood by taking into account just three physical principles: (1) an axial PD-oriented signal (tissue shear) that acts on differently oriented initial patterns, (2) the Sple-dependent coupling of Core PCP to Fat PCP that is stronger than the axial signal, and (3) the tendency of Core PCP domains to align with each other. Thus, while Sple-dependent coupling of Core to Fat PCP contributes importantly to the hair polarity patterns seen in Sple-overexpressing wings (and Pk mutant wings), it acts in the context of these other factors and the resulting patterns cannot be understood quantitatively without including them.

While hair polarity in *pk* wings is still guided by Core PCP, this system loses polarity in *fz* and *stbm* mutants [33]. Hair patterns in these mutants are oriented directly by Fat PCP. Thus, both PCP systems can orient hairs (consistent with results in the abdomen [21]), but when these two systems disagree, Core PCP dominates. Strikingly, even in the absence of both PCP systems hairs align with each other

locally and form global patterns exhibiting new features never observed in either type of mutant alone. Overall, our findings suggest that tissue polarity relies on multiple self-contained mechanisms that can be flexibly linked to each other.

Experimental Procedures

A detailed description of the experimental procedures and theoretical analysis is given in the Supplemental Information.

Supplemental Information

Supplemental Information includes Supplemental Experimental Procedures, Supplemental Theoretical Procedures, seven figures, two tables, and five movies and can be found with this article online at http://dx.doi.org/10.1016/j.cub.2014.08.005.

References

1. Goodrich, L.V., and Strutt, D. (2011). Principles of planar polarity in animal development. Development *138*, 1877–1892.

2. Baena-López, L.A., Baonza, A., and García-Bellido, A. (2005). The orientation of cell divisions determines the shape of Drosophila organs. Curr. Biol. *15*, 1640–1644.

3. Mao, Y., Tournier, A.L., Bates, P.A., Gale, J.E., Tapon, N., and Thompson, B.J. (2011). Planar polarization of the atypical myosin Dachs orients cell divisions in Drosophila. Genes Dev. *25*, 131–136.

4. Gubb, D., and García-Bellido, A. (1982). A genetic analysis of the determination of cuticular polarity during development in Drosophila melanogaster. J. Embryol. Exp. Morphol. *68*, 37–57.

5. Doyle, K., Hogan, J., Lester, M., and Collier, S. (2008). The Frizzled Planar Cell Polarity signaling pathway controls Drosophila wing topography. Dev. Biol. *317*, 354–367.

6. Waddington, C.H. (1939). Preliminary Notes on the Development of the Wings in Normal and Mutant Strains of Drosophila. Proc. Natl. Acad. Sci. USA *25*, 299–307.

7. Aigouy, B., Farhadifar, R., Staple, D.B., Sagner, A., Röper, J.C., Jülicher, F., and Eaton, S. (2010). Cell flow reorients the axis of planar polarity in the wing epithelium of Drosophila. Cell *142*, 773–786.

8. Classen, A.K., Anderson, K.I., Marois, E., and Eaton, S. (2005). Hexagonal packing of Drosophila wing epithelial cells by the planar cell polarity pathway. Dev. Cell *9*, 805–817.

9. Matis, M., and Axelrod, J.D. (2013). Regulation of PCP by the Fat signaling pathway. Genes Dev. *27*, 2207–2220.

10. Ambegaonkar, A.A., Pan, G., Mani, M., Feng, Y., and Irvine, K.D. (2012). Propagation of Dachsous-Fat planar cell polarity. Curr. Biol. *22*, 1302–1308.

11. Bosveld, F., Bonnet, I., Guirao, B., Tlili, S., Wang, Z., Petitalot, A., Marchand, R., Bardet, P.L., Marcq, P., Graner, F., and Bellaïche, Y. (2012). Mechanical control of morphogenesis by Fat/Dachsous/Four-jointed planar cell polarity pathway. Science *336*, 724–727.

12. Brittle, A., Thomas, C., and Strutt, D. (2012). Planar polarity specification through asymmetric subcellular localization of Fat and Dachsous. Curr. Biol. *22*, 907–914.

13. Tree, D.R., Shulman, J.M., Rousset, R., Scott, M.P., Gubb, D., and Axelrod, J.D. (2002). Prickle mediates feedback amplification to generate asymmetric planar cell polarity signaling. Cell *109*, 371–381.

14. Adler, P.N., Charlton, J., and Liu, J. (1998). Mutations in the cadherin superfamily member gene dachsous cause a tissue polarity phenotype by altering frizzled signaling. Development *125*, 959–968.

15. Hogan, J., Valentine, M., Cox, C., Doyle, K., and Collier, S. (2011). Two frizzled planar cell polarity signals in the Drosophila wing are differentially organized by the Fat/Dachsous pathway. PLoS Genet. *7*, e1001305.

16. Gubb, D., Green, C., Huen, D., Coulson, D., Johnson, G., Tree, D., Collier, S., and Roote, J. (1999). The balance between isoforms of the prickle LIM domain protein is critical for planar polarity in Drosophila imaginal discs. Genes Dev. *13*, 2315–2327.

17. Sagner, A., Merkel, M., Aigouy, B., Gaebel, J., Brankatschk, M., Jülicher, F., and Eaton, S. (2012). Establishment of global patterns of planar polarity during growth of the Drosophila wing epithelium. Curr. Biol. *22*, 1296–1301.

18. Lawrence, P.A., Casal, J., and Struhl, G. (2004). Cell interactions and planar polarity in the abdominal epidermis of Drosophila. Development *131*, 4651–4664.

19. Valentine, M., and Collier, S. (2011). Planar cell polarity and tissue design: Shaping the Drosophila wing membrane. Fly (Austin) *5*, 316–321.

20. Simon, M.A. (2004). Planar cell polarity in the Drosophila eye is directed by graded Four-jointed and Dachsous expression. Development *131*, 6175–6184.

21. Casal, J., Lawrence, P.A., and Struhl, G. (2006). Two separate molecular systems, Dachsous/Fat and Starry night/Frizzled, act independently to confer planar cell polarity. Development *133*, 4561–4572.

22. Donoughe, S., and DiNardo, S. (2011). dachsous and frizzled contribute separately to planar polarity in the Drosophila ventral epidermis. Development *138*, 2751–2759.

23. Ishikawa, H.O., Takeuchi, H., Haltiwanger, R.S., and Irvine, K.D. (2008). Four-jointed is a Golgi kinase that phosphorylates a subset of cadherin domains. Science *321*, 401–404.

24. Brittle, A.L., Repiso, A., Casal, J., Lawrence, P.A., and Strutt, D. (2010). Four-jointed modulates growth and planar polarity by reducing the affinity of dachsous for fat. Curr. Biol. *20*, 803–810.

25. Mao, Y., Rauskolb, C., Cho, E., Hu, W.L., Hayter, H., Minihan, G., Katz, F.N., and Irvine, K.D. (2006). Dachs: an unconventional myosin that functions downstream of Fat to regulate growth, affinity and gene expression in Drosophila. Development *133*, 2539–2551.

26. Yang, C.H., Axelrod, J.D., and Simon, M.A. (2002). Regulation of Frizzled by fat-like cadherins during planar polarity signaling in the Drosophila compound eye. Cell *108*, 675–688.

27. Zeidler, M.P., Perrimon, N., and Strutt, D.I. (2000). Multiple roles for four-jointed in planar polarity and limb patterning. Dev. Biol. *228*, 181–196.

28. Casal, J., Struhl, G., and Lawrence, P.A. (2002). Developmental compartments and planar polarity in Drosophila. Curr. Biol. *12*, 1189–1198.

29. Harumoto, T., Ito, M., Shimada, Y., Kobayashi, T.J., Ueda, H.R., Lu, B., and Uemura, T. (2010). Atypical cadherins Dachsous and Fat control dynamics of noncentrosomal microtubules in planar cell polarity. Dev. Cell *19*, 389–401.

30. Shimada, Y., Yonemura, S., Ohkura, H., Strutt, D., and Uemura, T. (2006). Polarized transport of Frizzled along the planar microtubule arrays in Drosophila wing epithelium. Dev. Cell *10*, 209–222.

31. Schwank, G., Tauriello, G., Yagi, R., Kranz, E., Koumoutsakos, P., and Basler, K. (2011). Antagonistic growth regulation by Dpp and Fat drives uniform cell proliferation. Dev. Cell *20*, 123–130.

32. Matakatsu, H., and Blair, S.S. (2004). Interactions between Fat and Dachsous and the regulation of planar cell polarity in the Drosophila wing. Development *131*, 3785–3794.

33. Strutt, D., and Strutt, H. (2007). Differential activities of the core planar polarity proteins during Drosophila wing patterning. Dev. Biol. *302*, 181–194.

34. Taylor, J., Abramova, N., Charlton, J., and Adler, P.N. (1998). Van Gogh: a new Drosophila tissue polarity gene. Genetics *150*, 199–210.

35. Venema, D.R., Zeev-Ben-Mordehai, T., and Auld, V.J. (2004). Transient apical polarization of Gliotactin and Coracle is required for parallel alignment of wing hairs in Drosophila. Dev. Biol. *275*, 301–314.

36. Ma, D., Yang, C.H., McNeill, H., Simon, M.A., and Axelrod, J.D. (2003). Fidelity in planar cell polarity signalling. Nature *421*, 543–547.

The Balance of Prickle/Spiny-Legs

Isoforms Controls the Amount of Coupling

between Core and Fat PCP Systems

Matthias Merkel, Andreas Sagner, Franz Sebastian Gruber, Raphael Etournay, Corinna Blasse, Eugene Myers, Suzanne Eaton, and Frank Jülicher
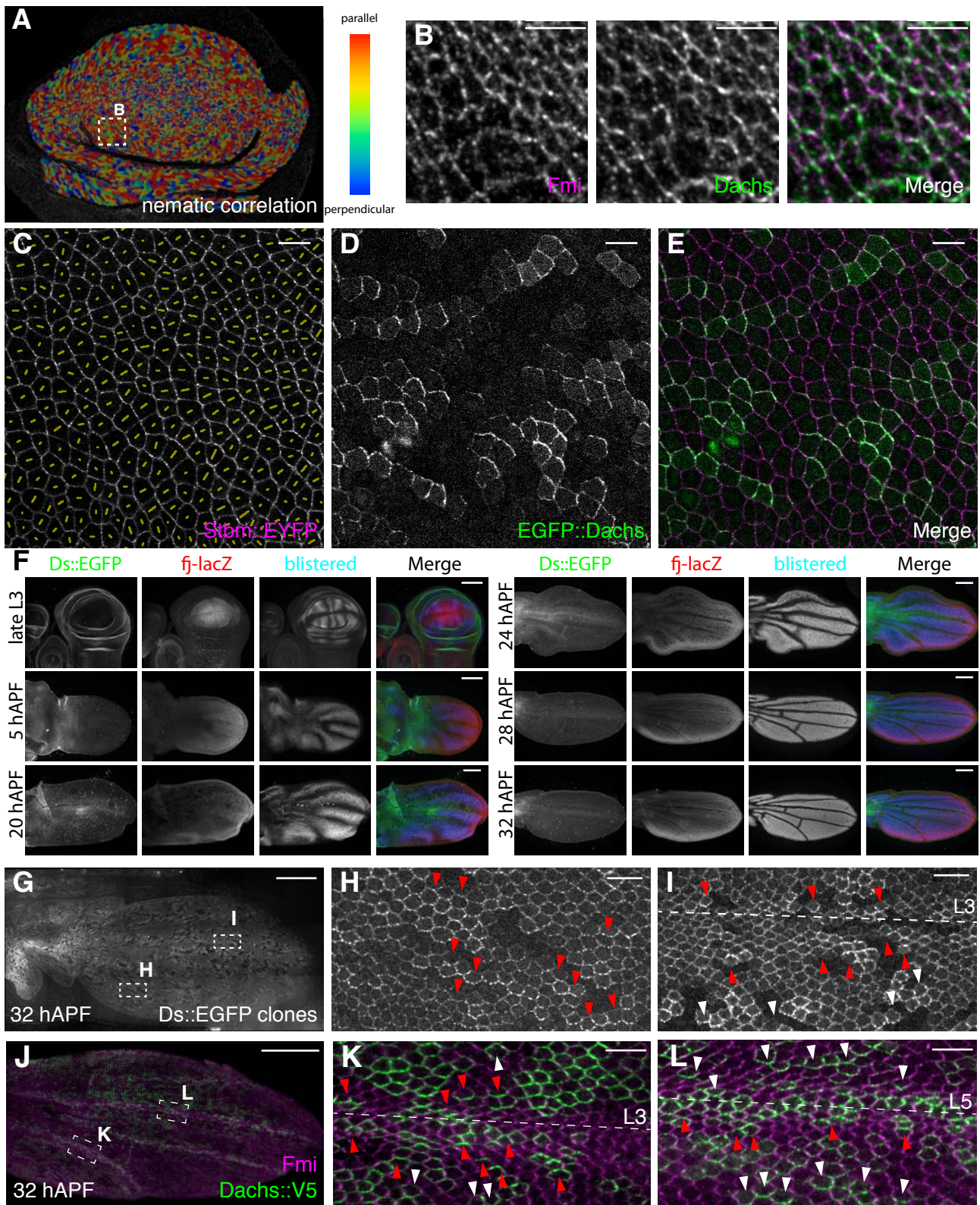
Figure S1 (to Figure 1): Evolution of Core PCP and Fat PCP during Drosophila wing development

(A) Correlation between Fmi and Dachs nematics in individual cells in the wing disc shown in Figures 1A and 1B. Red indicates parallel, blue perpendicular alignment of nematics.

(B) Higher magnification view of Fmi and Dachs staining in the boxed region in panel A. Note that Fmi and Dachs are similarly polarized but do not colocalize in punctate structures at the cell membrane.

(C-E) Single cell Stbm::EYFP nematics (C, Stbm::EYFP magenta in E) and EGFP::Dachs clones (D, green in E) in a pupal wing at 16 hAPF.

(F) Development of Ds and Fj gradients during wing development. To visualize the Ds gradient, a homologous recombinant expressing Ds::EGFP from the endogenous ds locus was used. Graded *fj* expression was visualized using a previously described lacZ insertion reflecting endogenous *fj* expression. Localization of wing veins was visualized by staining for blistered, a transcription factor that is only expressed in intervein cells.

(G-I) Analysis of Ds polarity by induction of Ds::EGFP expressing clones in a wild type background. (L) Clones in the fifth wing cell reveal Ds polarizes along the AP axis of each cell towards the wing margin (red arrowheads). (M) Clones reveal that Ds polarizes towards the L3 vein (indicated by the dashed line) on both sides of the vein (red arrowheads). Furthermore, note the switch of Ds polarity at larger distance from the L3 vein (white arrowheads).

(J-L) Flipping of Dachs polarity (red arrowheds) around longitudinal veins L3 (K) and L5 (L) revealed by Dachs::V5 expressing clones (green) in a pupal wing at 32 hAPF. Similar to Ds, Dachs polarity also flips at larger distance from the vein (white arrowheads). Furthermore, note the perpendicular polarization of Dachs and Fmi (magenta).

Scale bars = 5 µm (B), 10 µm (C-E,H,I,K,L), and 100 µm (F,G,J)
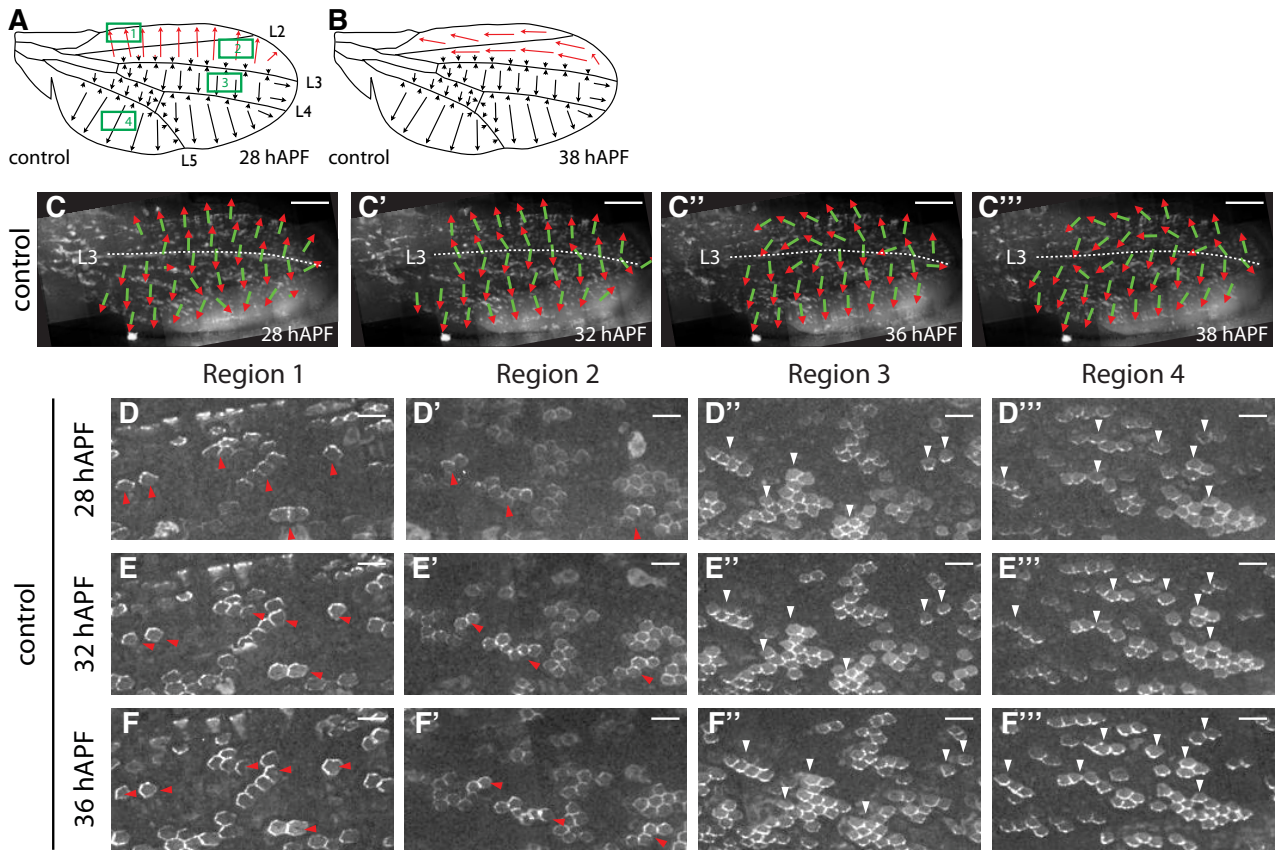
Figure S2 (to Figure 2): Late reorientation of Fat PCP using EGFP::Dachs clones as marker

(A-B) Schemes indicating reorientation of the Fat PCP pattern in wild type between 28 (A) and 38 hAPF (B).

(C-C''') Quantified EGFP::Dachs polarity in pupal wings at 28 (C), 32 (C'), 36 (C'') and 38 hAPF (C''') (Supplemental Experimental Procedures, Section 6).

(D-F''') Higher magnification views of the boxed regions in panel A (same wing as in C-C''') at 28 (D-D'''), 32 (E-E''') and 36 hAPF (F-F'''). Note that EGFP::Dachs polarity aligns with the PD axis anterior to L3 (red arrowheads in D-F').

Scale bars = 100 µm (C-C''') and 10 µm (D-F''')
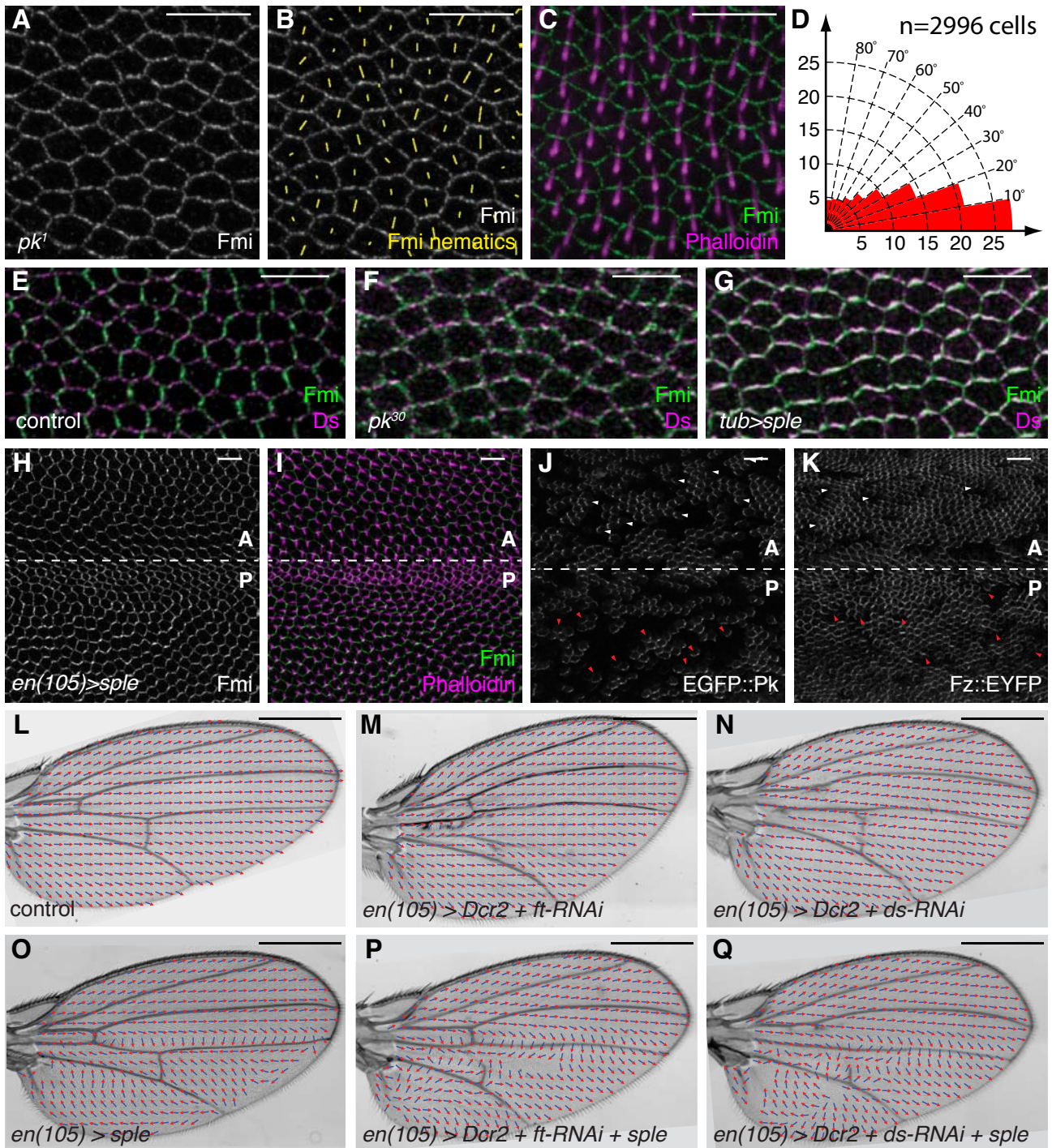
Figure S3 (to Figure 3): Analysis of Fat and Core PCP in *pk⁻* and Sple overexpression

(A-D) Residual Fmi polarity (A, single cell nematics in B, green in C) correlates with hair polarity (magenta in C) in pk^1 mutants at 32 hAPF. (D) Distribution of minimal angles between Fmi nematics and hair polarities of the same cells in pk^1 mutant pupal wings at 32 hAPF. For this analysis angles between Fmi nematics and hair polarities were measured in 2996 cells from 4 wings between the L3 and L4 veins and distal to the posterior cross vein.

(E-G) Comparison of Fmi (green) and Ds (magenta) polarity in wild type (E), pk^{30} (F) and *tub>sple* (G) in the fifth cell of pupal wings at 32 hAPF. Note that Fmi and Ds polarity are nearly perpendicular in wild type (E), but are parallel in pk^{30} (F) and *tub>sple* (G).

(H-K) Sple over-expression reverses the vector direction of the Core PCP system. (H,I) Hair polarity correlates with the pattern of Fmi polarization in the anterior and posterior compartment of *en(105)>sple* pupal wings at 32 hAPF. (J,K) EGFP::Pk (J) and Fz::EYFP (K) clones reveal reversal of Pk and Fz polarity in the posterior compartment of *en(105)>sple* pupal wings at 32 hAPF (red arrowheads).

(L-N) Quantified hair polarity in wild type (L), *en(105)>Dcr2 ft-RNAi* (M) and *en(105)>Dcr2 ds-RNAi* (N) adult wings. Note that knock-down of *ds* and *ft* in the posterior compartment does not cause PCP phenotypes.

(O) Quantified hair polarity in *en(105)>sple* adult wings. Sple overexpression in the posterior compartment causes a reversal of wing hairs.

(P,Q) Knock-down of *ft* (P) and *ds* (Q) rescues the hair polarity phenotype caused by *en(105)>sple* throughout most of the posterior compartment.

Scale bars = 10 μm (A-C,E-K) and 500 μm (L-Q)
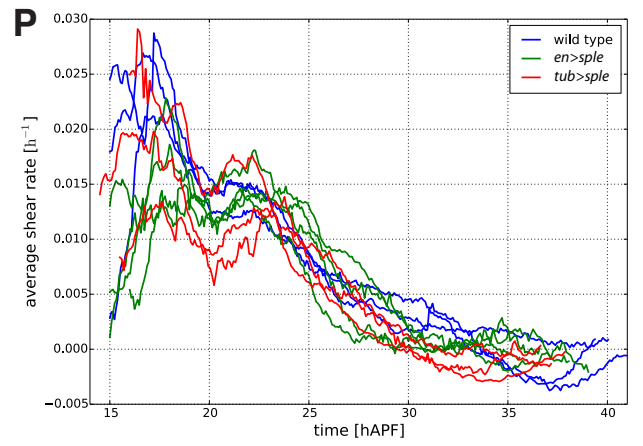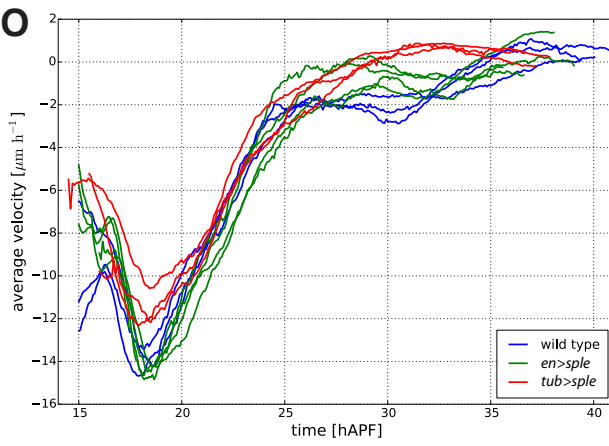
J *pk-sple locus (Chr2R: 3,038,207-3,110,885)*

pk   *sple*   *sple* probeset   common probeset

N

sple probe   common probe   Merge

wild type eye disc

pk-sple^13 eye disc

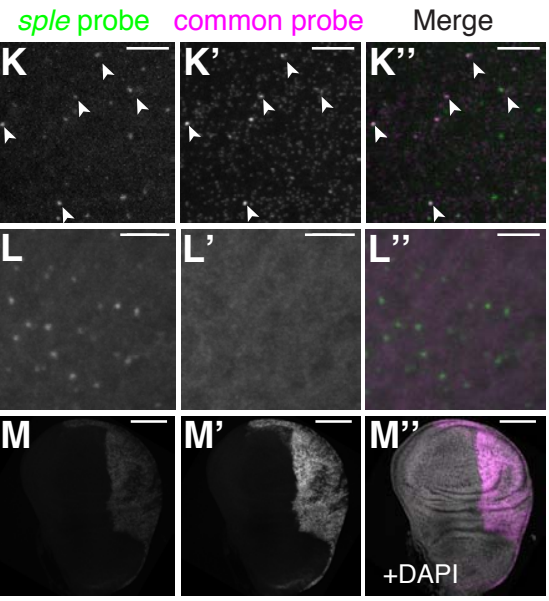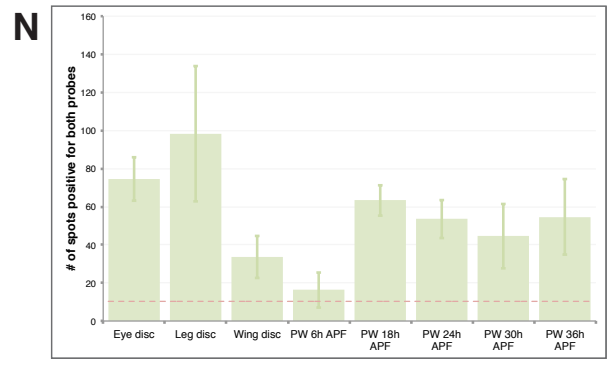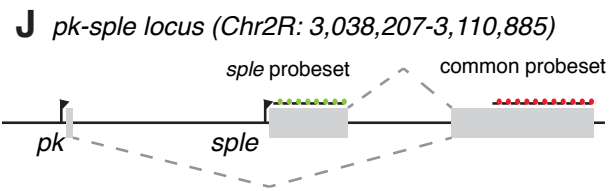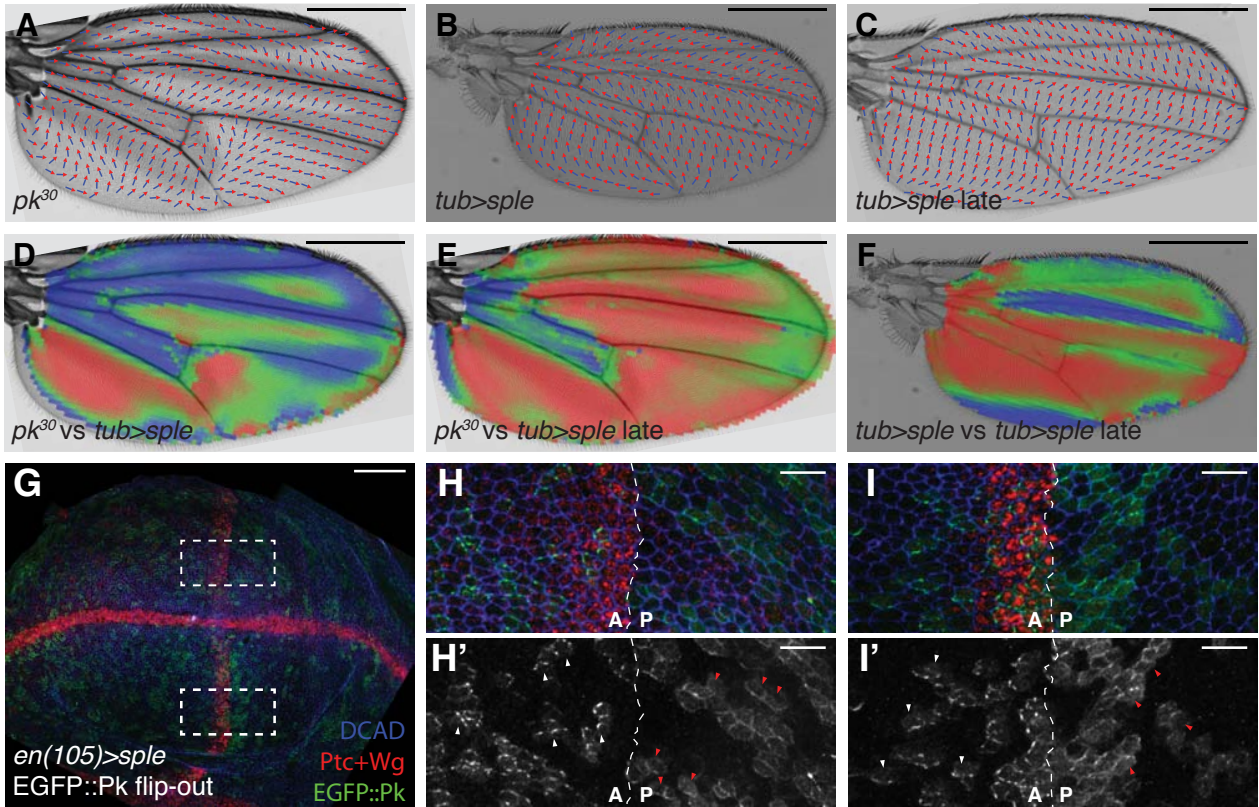*en(105)>sple* wing disc

+DAPI

O

P

Figure S4 (to Figure 4): Sple expression and its effect on hair polarity and tissue flows

(A-C) Quantification of hair polarity in pk^{30} (A), *tub>sple* (B), and *tub>sple* late (C) adult wings

(D-F) Quantitative comparison of adult wing hair polarities between pk^{30} and *tub>sple* (D), pk^{30} and *tub>sple* late (E), and *tub>sple* and *tub>sple* late (F). Red indicates parallel, blue antiparallel alignment of wing hairs. Note that the late ubiquitous overexpression of Sple mimics the pk^- hair polarity much better than the continuous Sple overexpression (compare D and E).

(G-I') Third instar wing disc of *en(105)>sple* with EGFP::Pk clones to map the direction of Core PCP stained for E-Cadherin (blue in G-I), Wg and Ptc (red in G-I) and EGFP (green in G-I, grayscale in H' and I'). (H-I') show higher magnifications of regions around the AP compartment boundary (dashed line in H-I') in the ventral (H,H') and dorsal compartment (I,I') of the wing disc shown in G. EGFP::Pk polarizes towards the proximal cell side in the anterior compartment (white arrowheads in H',I') and towards the distal cell side in the posterior compartment (red arrowheads in H',I').

(J) Scheme explaining smFISH experiments. Depicted is the structure of the *pk-sple* locus. *sple* and *pk* transcripts contain alternative 5' exons generated from alternative transcription start sites. To visualize only *sple* transcripts, a set of smFISH probes was designed against the *sple*-specific exon (green dots). To visualize both *pk* and *sple* transcripts, we designed a probe set targeting exons shared by *pk* and *sple* (red dots).

(K-L'') Double *in-situ* hybridizations with *sple*-specific (K,L and K'',L'' green) and common probes (K',L' and K'',L'' magenta) in wild type (K-K'') and pk-$sple^{13}$ (L-L'') eye imaginal discs. Under wild type conditions both probes detect the same transcripts (arrowheads). In pk-$sple^{13}$ mutants the common probe set does not detect transcripts (L'). In contrast, transcripts containing the *sple*-specific exon are still detected in this mutant (L). This suggests that the endpoint of the pk-$sple^{13}$ deletion lies between these regions.

(M-M'') Both probe sets detect elevated transcript levels in the posterior compartment of *en(105)>sple* wing discs.

(N) Quantification of co-localizing *sple* and common probe spots. Shown are the average values and standard deviation of leg disc, eye disc, wing disc as well as pupal wings staged between 6-36h APF. The red dotted line represents the background level detected in pk-$sple^{13}$ mutants.

(O,P) Quantified average velocity field (O) and average shear field (P) in wild type wings (blue curves), *en(105)>sple* wings (green curves), and *tub>sple* wings (red curves) (Supplemental Experimental Procedures, Section 11). Shown is the tensor component that is parallel to vein L3, respectively.

Scale bars = 500 µm (A-F), 100 µm (G, M-M''), 10 µm (H-I') and 5 µm (K-L'')

Alternative model: Sple over-expression flips the sign of kv

experiment: adult wing hair pattern

theory: predicted Core PCP pattern at wing hair outgrowth

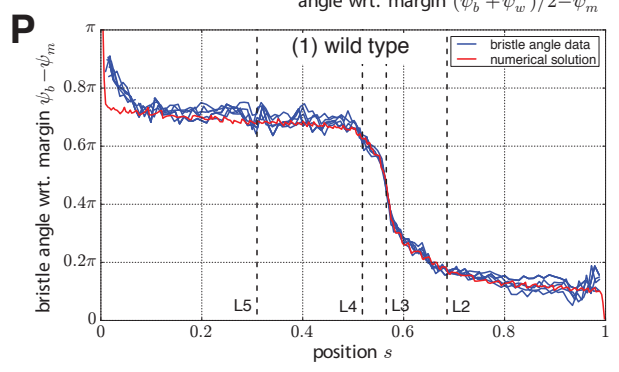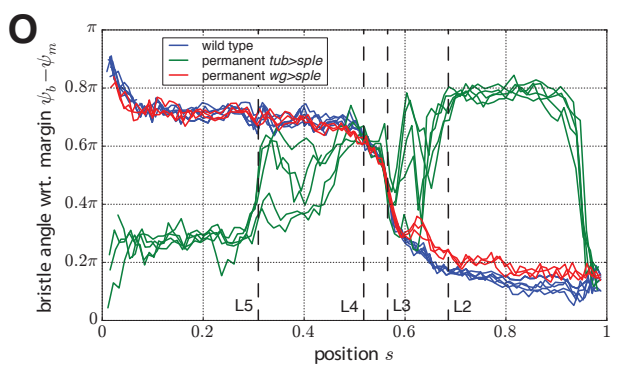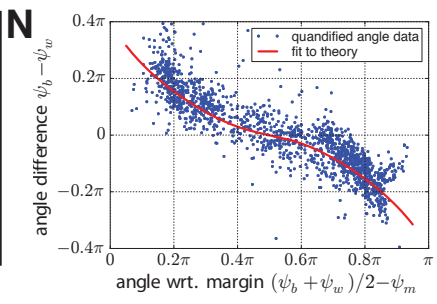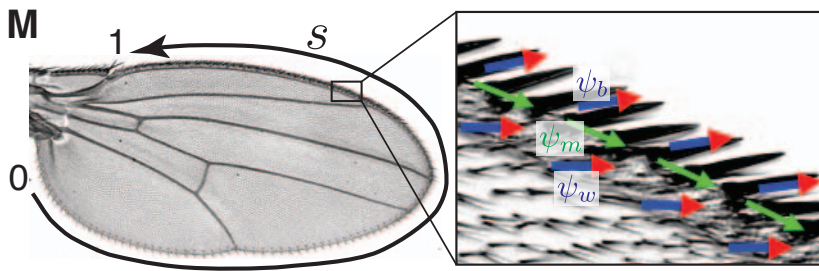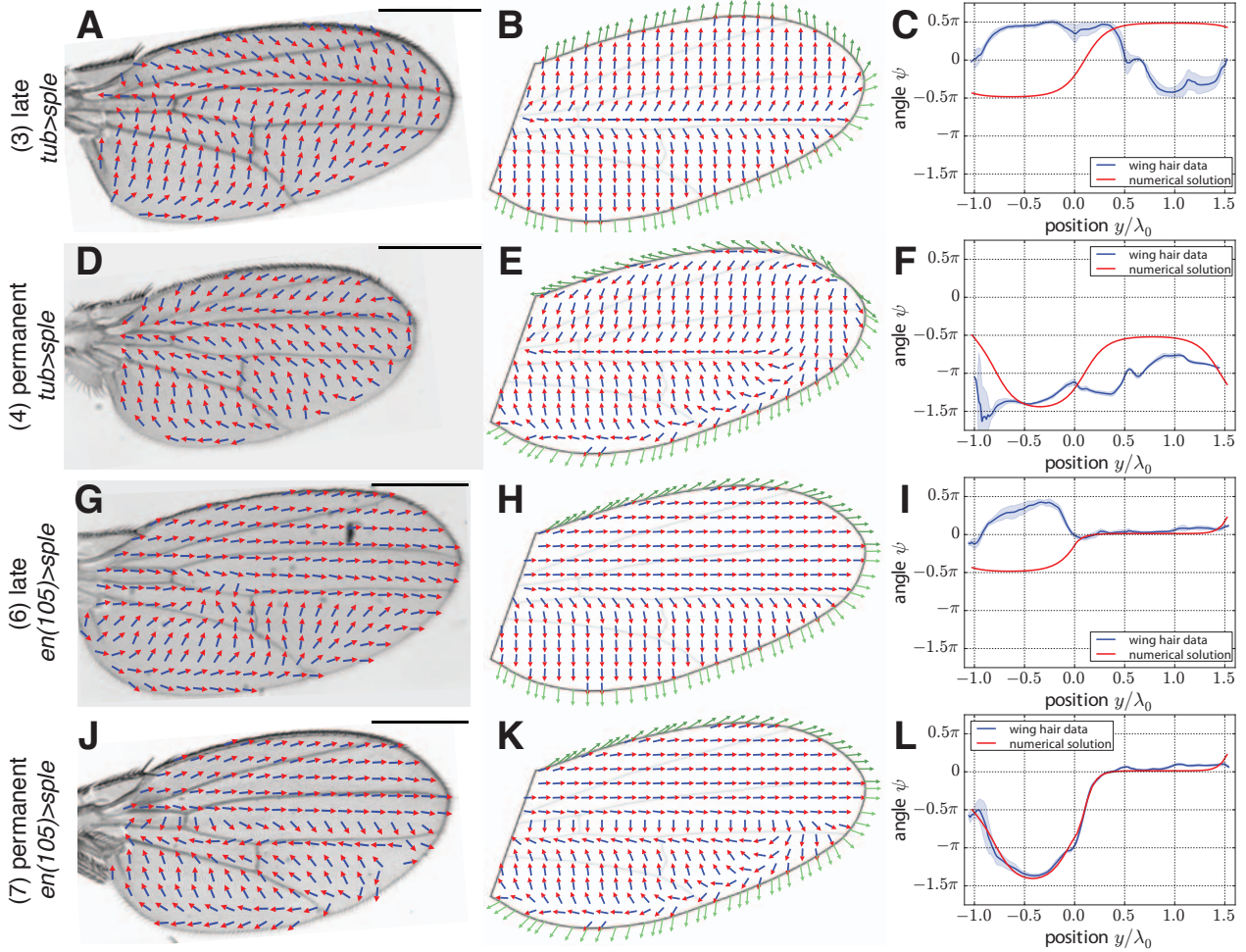**angle profile:** comparison of experiment and theory

Figure S5 (to Figure 5): An alternative model for Sple over-expression, and wing margin bristle angles can be predicted by our physical theory

(A-L) Results of our physical theory for the alternative model (Table S2, model B). Quantified wing hair patterns (first column) are compared to numerical solutions of Eq. (1) at the time of wing hair outgrowth (second column). In the numerical solutions of Eq. (1), bulk polarity (blue and red arrows) as well as the direction of wing margin bristles (green arrows) are indicated (see Supplemental Theoretical Procedures, Section 2). Third column: Direct comparison of experimental (blue solid lines) and theoretical (red solid lines) polarity patterns. We plot angles for both along the line shown in red in Figure 4G. For the experimental curves, we quantified the hair polarity of at least eight wings for each condition. The blue-hatched region indicates the circular standard deviation of the quantified wing hair angles (Supplemental Experimental Procedures, Section 9). The theoretical curves correspond to the respective polarity patterns shown in panels B,E,H,K. The numerical solutions for the wild type and the early *tub>sple* and *en(105)>sple* conditions are the same as for model A (see Figure 5B,E,N, respectively).

(M) Quantification of bristle angles ψ_b along the wing margin (Supplemental Experimental Procedures, Section 10). Also, we quantified the margin angle ψ_m and the wing hair angle close to the margin ψ_w. We parameterized the margin by the coordinate s, which takes values between zero (posterior indentation at the hinge blade interface) and one (anterior indentation at the hinge blade interface).

(N) Plot of the difference between margin bristle angle and wing hair angle against the average of both with respect to the wing margin. The experimental data shown here are taken from the range between the posterior indentation at the hinge blade interface and the distal end of vein L3 ($s \approx 0 \dots 0.55$) and include wings from all seven conditions examined. These data are fitted to the boundary condition of our physical theory in order to determine model parameters (Supplemental Theoretical Procedures, Section 2).

(O) Comparison of quantified margin bristle angle profiles for wild type case, permanent ubiquitous Sple over-expression (permanent *tub>sple*), and Sple over-expression only at the wing margin (*wg>sple*). The dashed vertical lines indicate the positions of vein ends. For each wing, the coordinate s is rescaled such that the positions of vein ends match among all wings (Supplemental Experimental Procedures, Section 10).

(P) Comparison of the quantified margin bristle angle profile in wild type wings (blue curves) with the theoretically obtained curve (red curve). The theoretical curve corresponds to the margin polarity of the final state of the numerical solution of Eq. (1) (green arrows in Figure 5B).

Scale bars = 500 µm (A,D,G,J)
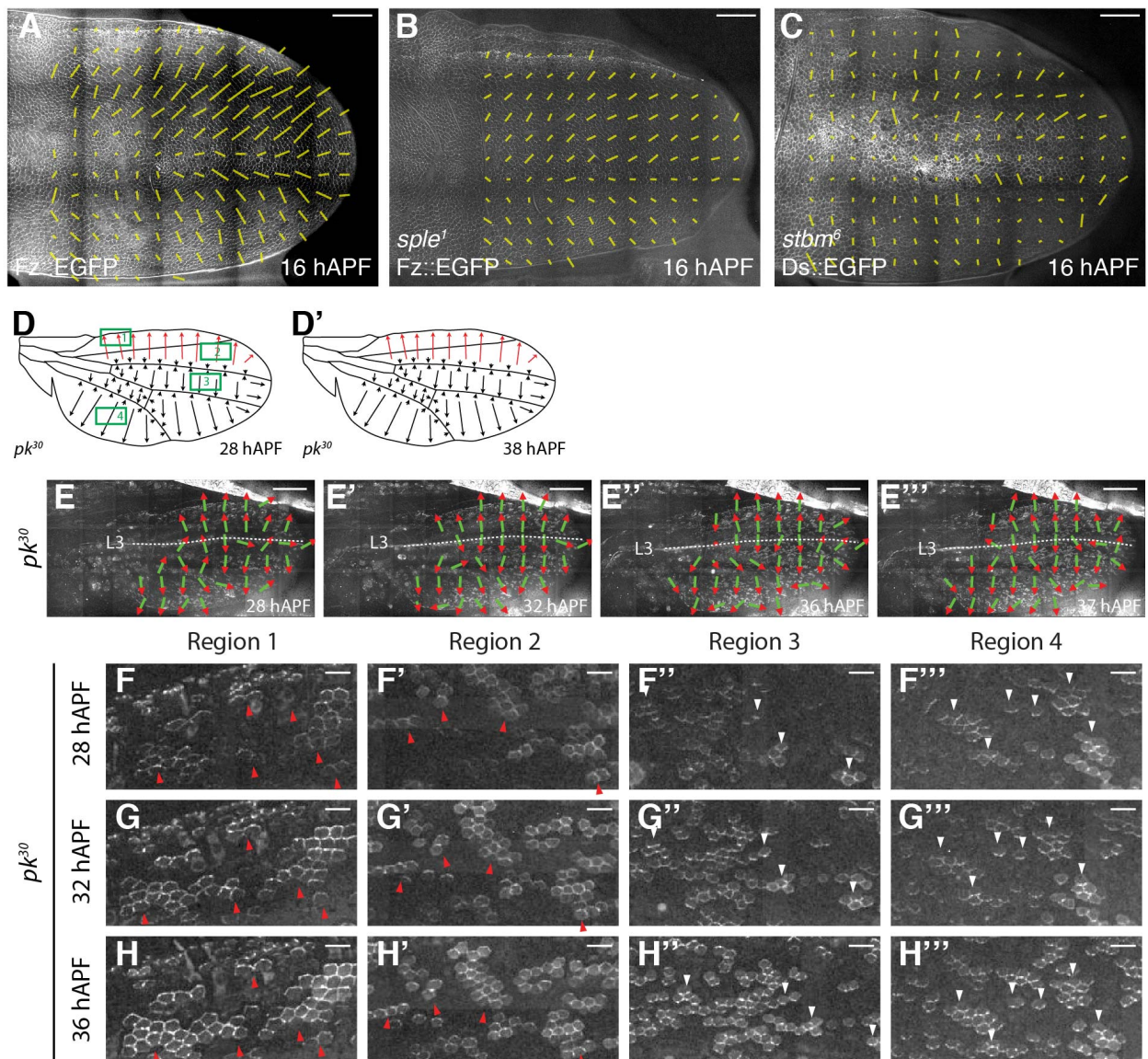
Figure S6 (to Figure 6): Late reorientation defects of Fat PCP in *pk⁻*

(A,B) Fz::EGFP coarse-grained nematics at 16 hAPF in control (A) and *sple¹* (B).

(C) Ds::EGFP coarse-grained nematics at 16 hAPF in a *stbm⁶* mutant.

(D,D') Schemes indicating reorientation of the Fat PCP pattern in *pk* mutants between 28 (D) and 38 hAPF (D').

(E-E''') Quantified EGFP::Dachs polarity in *pk¹/pk³⁰* pupal wings at 28 (E), 32 (E'), 36 (E'') and 37 hAPF (E''') (Supplemental Experimental Procedures, Section 6). Note that EGFP::Dachs polarity does not reorient anterior to L3 (compare to S2C-C''').

(F-H''') Higher magnification views of the boxed regions in panel D (same wing as in E-E''') at 28 (F-F'''), 32 (G-G''') and 36 hAPF (H-H'''). Note that EGFP::Dachs polarity does not align with the PD axis anterior to L3 (red arrowheads in F-H').

Scale bars = 50 μm (A-C), 100 μm (E-E''') and 10 μm (F-G''')
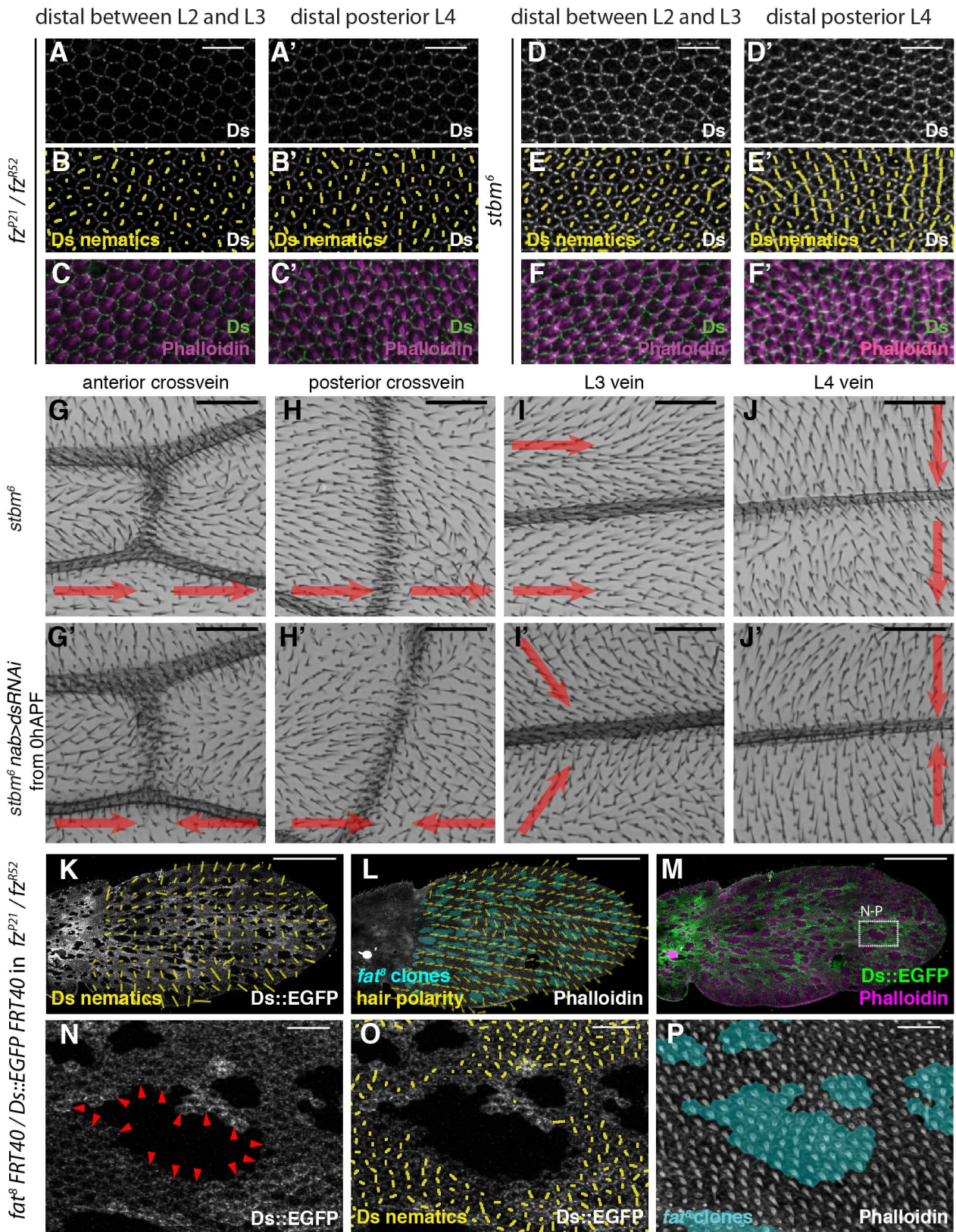
Figure S7 (to Figure 7): Ds polarity correlates with hair polarity in *stbm* and *fz* mutants

(A-F'') Ds staining (A-F', green in C,C',F,F'), Ds polarity nematics (B,B',E,E') and hair polarity (magenta in C,C',F,F') distal between L2 and L3 (A-F) or distal posterior to the L4 vein (A'-F') in *fz^{P21}* / *fz^{R52}* (A-C') or *stbm^6* (D-F') pupal wings at 35 hAPF. Note that orientation of Ds nematics correlates with hair orientation.

(G-J') Higher magnification views of hair polarity around the anterior and posterior crossveins (G,G',K,K') and the L3 and L4 veins (I,I',J,J') in *stbm^6* (G-J) and *stbm^6 nab>ds-RNAi* from 0 hAPF (G'-J'). Red arrowheads indicate the orientation of wing hairs. Note that hair polarity flips across all veins when Fat PCP is perturbed in *stbm^6* mutants but not in *stbm^6* mutants with intact Fat PCP system.

(K-M) Pupal wing at 35 hAPF containing *ft^8* clones labeled by absence of Ds::EGFP in a *fz^{P21} / fz^{R52}* background stained for EGFP (K, green in M) and Phalloidin (L, magenta in M). (K) shows additionally the pattern of coarse-grained Ds::EGFP nematics and (L) the quantified pattern of prehairs.

(N-P) Higher magnification views of the boxed region in (M). Note that Ds::EGFP localizes away from the *ft^8* clone border (red arrowheads in N). Further note that hairs still align between adjacent cells in *ft fz* double mutant tissue (blue patch in P).

Scale bars = 10 µm (A-F', Q-S), 50 µm (G-J') and 100 µm (K-P)

Table S1 (to Supplemental Theoretical Procedures): Fit parameter values $\lambda_{\text{wt}} = (\kappa_{\text{wt}}/2|k\nu_{\text{wt}}|)^{1/2}$ and $\mu_{\text{so}} = (\kappa_{\text{so}}/|\zeta_{\text{so}}|)^{1/2}$ obtained by fitting calculated one-dimensional orientation profiles to quantified averaged wing hair angle profiles (for details, see Supplemental Theoretical Procedures, Section 3). λ_0 denotes the half wing width (see Supplemental Experimental Procedures, Section 9.).

Case	$\lambda_{\text{wt}}/\lambda_0$	$\mu_{\text{so}}/\lambda_0$
(2) Early *tub>sple*	0.062	--
(5) Early *en(105)>sple*	0.071	--
(3) Late *tub>sple*	--	0.173
(4) Permanent *tub>sple*	--	0.388
(6) Late *en(105)>sple*	0.072	0.141
(7) Permanent *en(105)>sple*	0.070	0.158

Table S2 (to Figures 5, S5): Set of parameter values that can account for wild type and different mutant conditions, as shown in Figures 5 (model A) and S5A-L (model B). Lengths are defined with respect to the half wing width, λ_0. Also shown are initial conditions and parameters used for solving Eq. (1) for the conditions discussed in the main text. Anterior (posterior) parameters denote the parameters for the region with $y > 0$ ($y < 0$), corresponding to the anterior (posterior) compartment (compare Figure 4G). The parameters for solving Eq. (1) in a given region can be either wild type parameters ($k\nu_{\text{wt}}$, ζ_{wt}, and κ_{wt}) or Sple over-expression parameters ($k\nu_{\text{so}}$, ζ_{so}, and κ_{so}).

Model	$k\nu_{\text{wt}}$ $[\text{h}^{-1}]$	ζ_{wt} $[\text{h}^{-1}]$	κ_{wt} $[\lambda_0{}^2\,\text{h}^{-1}]$	$k\nu_{\text{so}}$ $[\text{h}^{-1}]$	ζ_{so} $[\text{h}^{-1}]$	κ_{so} $[\lambda_0{}^2\,\text{h}^{-1}]$
Model A	-0.1	0	0.98×10^{-3}	-0.1	-0.4	10.24×10^{-3}
Model B	-0.1	0	0.98×10^{-3}	0.1	0	3.92×10^{-3}

Condition	Initial condition	Anterior parameters	Posterior parameters	Figure
(1) wild type	Figure 4J	wild type	wild type	5A-C
(2) early *tub>sple*	Figure 4K	wild type	wild type	5D-F
(3) late *tub>sple*	Figure 4J	Sple over-expression	Sple over-expression	5G-I
(4) permanent *tub>sple*	Figure 4K	Sple over-expression	Sple over-expression	5J-L
(5) early *en(105)>sple*	Figure 4L	wild type	wild type	5M-O
(6) late *en(105)>sple*	Figure 4J	wild type	Sple over-expression	5P-R
(7) permanent *en(105)>sple*	Figure 4L	wild type	Sple over-expression	5S-U

Supplemental Experimental Procedures

1. Fly Strains

Alleles used (pk^1, pk^{30}, pk-$sple^{13}$, $sple^1$, fz^1, fz^{P21}, fz^{R52}, $stbm^6$, ft^1, ft^8) were described previously [S1-5]. *nab-Gal4 and tub*-Gal4 are available from the Bloomington stock center. *en(105)*-Gal4 is a posterior compartment specific Gal4 line and was described previously [S6]. *UAS-sple, UAS-dachs::V5*, and E-Cadherin::EGFP fly lines were described previously [S2, S7, S8]. *UAS-Dcr2* flies are available from VDRC and the Bloomington stock center. *UAS-ds RNAi* (#36219) and *UAS-ft RNAi* (#9396) lines were obtained from VDRC. The Ds::EGFP homologous recombinant, *act5c>stop>EGFP::dachs*, *act5c>stop>fz::EYFP*, *act5c>stop>stbm::EYFP* and *act5c>stop>EGFP::pk* fly lines were described previously and were kindly shared by David Strutt [S9-11]. Patches of tissue expressing the respective fusion protein were generated by crossing fly lines to a Flippase under the control of a heat-shock promoter, and heat-shocking flies at the beginning of pupal development. Pupae were heat shocked for between 1.5 and 3 minutes in a water bath set to 37 degrees.

Stbm::EYFP was created by fusing EYFP directly to the Stbm cDNA under control of a polyubiquitin promoter. Site-specific transgenesis into the VK0033 landing site was performed as previously described [S12].

Fly lines expressing EGFP::Pk and Fz::EGFP under endogenous regulatory sequences were generated by Recombination Mediated Cassette Exchange (RMCE) of a Minos Mediated Integration Cassette (MiMIC) element as described in [S13]. To generate the EGFP::Pk protein trap, we replaced the MiMIC of Bloomington line # 36156 using pBS-KS-attB1-2-PT-SA-SD-2-EGFP-FlAsH-StrepII-TEV-3x-Flag (available on DGRC, # 1314). To generate the Fz::EGFP protein trap, we cloned a region that includes 2.2 kb upstream and the last exon of *fz* fused with EGFP-FlAsH-StrepII-TEV-3x-Flag and followed by a region that is 1.4 kb downstream of the *fz* stop codon into pBS-KS-attB1-2 (DGRC, # 1322). Using RMCE we replaced the MiMIC of Bloomington line # 42184. Both fly lines are homozygous viable, and the fusion proteins localize asymmetrically in wing discs and throughout pupal wing development.

To control the spatiotemporal pattern of Sple over-expression, we utilized the Gal4/Gal80^{TS} system [S14] and the *en(105)*-Gal4 and *tub*-Gal4 driver lines. Gal80^{TS} repressesGal4-dependent transcription at 18 degrees but not at 29 degrees. To stop expression of Sple at different times, we shifted flies harboring UAS Sple and Gal80^{TS} combined with these different Gal4 drivers from 29 to 18 degrees. To initiate it at different times, we shifted from 29 to 18 degrees. Western blotting imaginal discs indicated that Sple protein levels increase approximately 4 hours after shifting to 29 degrees. Shifting from 29 to 18 degrees starts to reduce Sple protein levels after 4 hours, with a strong reduction after 8-12 hours (data not shown). For expression experiments denoted "early", flies were reared at 29 degrees and shifted 12 hAPF to 18 degrees. For expression experiments denoted "late", flies were reared at 18 degrees and shifted 30 hAPF to 29 degrees. Developmental timing depends on temperature, and these shifts were designed to alter Sple expression shortly before pupal tissue flows begin. For all experiments, continuous maintenance of flies at 18 degrees did not result in any hair

polarity phenotype and continuous maintenance at 29 degrees gave the same hair polarity phenotype as keeping flies of the same genotype except the *tub-Gal80^{TS}* transgene at 25 degrees. Flies downshifted at 6 hAPF had similar proximal-oriented hair polarity patterns to those downshifted at 12 hAPF (not shown).

2. Immunohistochemistry and smFISH

Pupal wings and wing discs were fixed and dissected on ice using PBS + 4% PFA. Washing and staining steps were performed in PBS + 0.1% Triton X-100. Tissues were mounted in Vectashield. Primary antibodies used are rabbit-anti-Fmi (1:200; [S15]), rabbit-anti-GFP (1:1000; Invitrogen), mouse-anti-DSRF (1:100; Millipore), mouse-anti-Ds2829 (1:1000; this study); mouse-anti-V5 (1:800; Invitrogen), mouse-anti-Arm (1:1000; DSHB), rat-anti-E-Cadherin (1:100; DSHB), rat-anti-Dachs (1:1000; [S10]) and chicken-anti-LacZ (1:2000, Abcam). Secondary antibodies used were anti-rabbit-Alexa488, anti-mouse-Alexa555, anti-rat-Alexa647 and anti-chicken-Alexa647. Alexa555 and Alexa647 conjugated Phalloidin were used 1:250 to label wing hairs. Mouse-anti-Ds2829 is a polyclonal antibody raised against amino acids 3142-3298 of Ds protein.

smFISH probes were ordered from Biosearch Technologies. The staining procedure was performed according to manufacturers protocol using 250 nM per probeset.

3. Image Acquisition

Images of antibody-stained samples were using an Olympus-FV-1000 point-scanning confocal microscope equipped with a programmable stage to allow multi-tile acquisition. Tissues were recorded with 5% overlap between adjacent tiles to allow subsequent stitching. Pupal wings were recorded with a resolution of 0.207 µm / Pixel, wing discs with a resolution of 0.069 µm / Pixel using a 60x oil immersion objective (NA = 1.35). A commonly available Fiji Plugin was used for stitching [S16]. Co-localization of common probe and *sple* probe spots in smFISH experiments were quantified using a Fiji Plugin described in [S17]. A corresponding region with 600x600 pixels and 2.5 µm in depth was used for analysis.

For life imaging, pupae were prepared as described previously [S18]. To quantify global Core PCP patterns at 16 hAPF, the entire wing blade was recorded using an Olympus-FV-1000 point-scanning confocal microscope. For quantification of global core PCP and Fat PCP patterns, pupal wings were imaged at cellular resolution every 20min (Stbm::EYFP) or 30min (all other movies) starting at 16h00APF. For quantifications of velocity and shear fields in control and *tub>sple* flies, wings were imaged ca. every 5min. Imaging was performed using an inverted confocal spinning disk microscope (Zeiss) equipped with a LCI Plan-Neofluar 63x 1.3 Imm Corr lens and a temperature control unit set to 25 degrees. Axiovision and custom Fiji macros were used for focus adjustment. The acquisition of 24 overlapping positions (Z-stacks, ~45 slices, 1um/slice) in 5min yielded a tiling of the entire wing. Time-lapse assembly was performed using a semi-automated pipeline described elsewhere (manuscript in preparation). In brief, Z-stacks of each position were first projected using a newly developed projection algorithm, which projects the apical band of monolayer epithelial tissues into 2D images, and stitched using Fiji [S16] to reconstitute the whole wing.

Adult wings were recorded with a wide field microscope (Zeiss Axiovert 200M) equipped with a Plan-Neofluar 10x objective. Multi-tile acquisitions were performed by using a Metamorph7.1 custom macro for automated scanning, stitching and z-projections (scan-slide and best-focus Metamorph modules). Imaging of cuticular ridges was performed using the same microscope with the adjustments described in [S19].

4. Image Projection

To quantify the asymmetric localization of PCP proteins in the entire wing, we developed a new projection algorithm that projects the level of the adherens junctions out of the stitched 3D images (manuscript in preparation). The algorithm splits the 3D volume into columns and determines for each column the most informative plane using the pixel intensity, variance and the surface smoothness. These planes define the pixels being projected onto the 2D image.

In more detail, the algorithm creates an initial height map by determining for each column the plane that includes the brightest pixels. This map is smoothed in regions where neighboring planes show such a big distance in the 3D volume that the junction would be biological implausible. To refine the plane selection, the algorithm divides each column into four pieces. Within these columns a substack is defined including a definite range of planes above and below the previously selected plane. In the last step, the plane with the highest variance is determined and its pixels are projected onto the 2D image.

After the height map has been calculated for one channel of a multi-channel input image, it can be reapplied to other channels of the image. To correct for small offsets between channels, we allow the plane chosen by the algorithm to differ by one z-section below and above the originally chosen plane. To project only wing hairs in Phalloidin-stained samples, we allowed the algorithm to pick the brightest plane between 2 and 5 z-sections above the z-section with brightest Fmi staining.

5. Quantification of cell polarity

For the quantification of cell polarity patterns in Figures 1-4, 6-7, S1, S3, S6, and S7, we used the same definition for cell polarity as in earlier work [S15], which we repeat here for clarity. Cells were segmented based on E-Cadherin staining as described previously [S20]. Polarity nematics are computed for each cell individually and are characterized by an axis and a magnitude and represented by a traceless, symmetric tensor

$$\boldsymbol{Q} = \begin{pmatrix} Q_1 & Q_2 \\ Q_2 & -Q_1 \end{pmatrix}$$

where the components Q_1 and Q_2 are defined by

$$Q_1 = \frac{1}{N} \int_0^{2\pi} I(\varphi) \cos(2\varphi) \, \mathrm{d}\varphi$$

$$Q_2 = \frac{1}{N} \int_0^{2\pi} I(\varphi) \sin(2\varphi) \, \mathrm{d}\varphi$$

$I(\varphi)$ is the intensity of PCP molecule fluorescence at the cell boundary pixel at the angle φ defined with respect to the cell center. The integrals are determined as discrete sums over the pixels of the cell

boundaries. The normalization constant N is defined by $N = \int_0^{2\pi} I(\varphi)\, d\varphi$. This normalization step makes the polarity measure insensitive to intensity variations in images.

6. Quantification of the vector polarity of stained clones without segmentation

We quantified the Ds::GFP clone polarities in Figures S2C-C''' and S6E-E''' without segmentation of cells. The main idea is to exploit the observation that the fluorescence intensity within a cell is slightly higher than outside of the cell. We first determine vectors $\boldsymbol{p}$ and $\boldsymbol{q}$, which are approximately normal to the clone boundary near the clone boundary. From the vector $\boldsymbol{p}$, we construct a polarity vector $\boldsymbol{P}$ of the clone, which depends on the PCP fluorescence intensity. We started from an image representing local PCP fluorescence intensities. The intensity at pixel position $\boldsymbol{r} = (x, y)$ is denoted by $I(\boldsymbol{r})$. For each pixel position $\boldsymbol{r}$, we defined a local polarity vector $\boldsymbol{q}(\boldsymbol{r})$ in the following way:

$$ \boldsymbol{q}(\boldsymbol{r}) = \sum_{\Delta r} \frac{\Delta \boldsymbol{r}}{\Delta r} \exp\left(-\frac{\Delta r^2}{\lambda_p{}^2}\right), $$

where the sum runs over the $f = 40\%$ darkest pixel intensities $I(\boldsymbol{r} + \Delta \boldsymbol{r})$ within a cutoff radius of $c = 20$ pixels around $\boldsymbol{r}$. The length scale λ_p is set to 10 pixels.

When $\boldsymbol{r}$ is a pixel at the boundary of a Ds::GFP clone, $\boldsymbol{q}(\boldsymbol{r})$ will usually point outside the clone in a direction normal to the clone boundary.

In order to construct a related vector $\boldsymbol{p}(\boldsymbol{r})$, we define for each pixel position $\boldsymbol{r}$ the symmetric, traceless tensor $\boldsymbol{n}(\boldsymbol{r})$:

$$ \boldsymbol{n}(\boldsymbol{r}) = \begin{pmatrix} n_1 & n_2 \\ n_2 & -n_1 \end{pmatrix} $$

with

$$ n_1(\boldsymbol{r}) = \sum_{\Delta r} I(\boldsymbol{r} + \Delta \boldsymbol{r}) \cos(2\phi_{\Delta r}) \exp\left(-\frac{\Delta r^2}{\lambda_n{}^2}\right) $$

$$ n_2(\boldsymbol{r}) = \sum_{\Delta r} I(\boldsymbol{r} + \Delta \boldsymbol{r}) \sin(2\phi_{\Delta r}) \exp\left(-\frac{\Delta r^2}{\lambda_n{}^2}\right), $$

where the sums run over all pixels with $\Delta \boldsymbol{r} = \Delta r (\cos \phi_{\Delta r}, \sin \phi_{\Delta r})$ within a cutoff radius of $\Delta r \leq c$. The length scale λ_n is set to 10 pixels. On a cell boundary, $\boldsymbol{n}(\boldsymbol{r})$ provides the direction of the cell boundary. In order to obtain the refined vector $\boldsymbol{p}(\boldsymbol{r})$, we project $\boldsymbol{q}(\boldsymbol{r})$ on the axis perpendicular to the axis of the nematic tensor $\boldsymbol{n}(\boldsymbol{r})$:

$$ p_i(\boldsymbol{r}) = q_i(\boldsymbol{r}) - \frac{1}{|\boldsymbol{n}(\boldsymbol{r})|} n_{ij}(\boldsymbol{r}) q_j(\boldsymbol{r}), $$

where $i, j \in \{x, y\}$ are dimension indices and Einstein convention is used. The norm of $\boldsymbol{n}(\boldsymbol{r})$ is defined by $|\boldsymbol{n}(\boldsymbol{r})| = (n_1{}^2 + n_2{}^2)^{1/2}$.

In order to construct $\boldsymbol{P}$, we first subtract the locally averaged pixel intensity from the pixel intensity at $\boldsymbol{r}$

$$ \Delta I(\boldsymbol{r}) = I(\boldsymbol{r}) - \frac{1}{N_c} \sum_{\Delta r} I(\boldsymbol{r} + \Delta \boldsymbol{r}), $$

where the sum runs over all N_c pixels within a cutoff radius of $\Delta r \leq c$. We define the clone polarity $\boldsymbol{P}$ as:

$$P = \sum_{r} [\Delta I(r)|n(r)|]^{1/2} p(r),$$

where the sum runs over all pixels r belonging to the clone with positive $\Delta I(r)$. We took the root of the prefactor in order to obtain a quantity that is linear in pixel intensity.

7. Quantification of hair polarity in adult wings

For the quantification of wing hair and ridge patterns in Figures 2, 5, 7, S3-S5, and S7, we quantified a local nematic based on anisotropies in the image. We follow a procedure similar to a method described in earlier work [S15]. However, we have modified the definition of the nematic tensor n representing local pixel correlations. In a grayscale image of an adult wing, we denote the pixel intensity at r by $I(r)$. For each pixel position $r = (x, y)$ within the blade, we define

$$n(r) = \begin{pmatrix} n_1 & n_2 \\ n_2 & -n_1 \end{pmatrix}$$

with

$$n_1(r) = I(r) \sum_{\Delta r} I(r + \Delta r) \cos(2\phi_{\Delta r}) \exp\left(-\frac{\Delta r^2}{\lambda^2}\right)$$

$$n_2(r) = I(r) \sum_{\Delta r} I(r + \Delta r) \sin(2\phi_{\Delta r}) \exp\left(-\frac{\Delta r^2}{\lambda^2}\right),$$

where the sums run over all pixels with $\Delta r = (\Delta x, \Delta y) = \Delta r(\cos \phi_{\Delta r}, \sin \phi_{\Delta r})$ within a cutoff radius of $\Delta r \leq 10$ pixels. The pixel intensity at r is denoted by $I(r)$. The length scale λ is set to 2 pixels.

In a second step, images were divided into boxes with a side length of 20 pixels. The nematic $n(r)$ defined at all pixels is averaged within each box. Thus, each box (with indices i, j) carries a nematic n_{ij}. The corresponding angle $\bar{\psi}_{ij}$ is given by

$$\cos(2\bar{\psi}_{ij}) = \frac{n_{ij,1}}{|n_{ij}|}$$

$$\sin(2\bar{\psi}_{ij}) = \frac{n_{ij,2}}{|n_{ij}|}$$

with $|n_{ij}| = \left(n_{ij,1}^2 + n_{ij,2}^2\right)^{1/2}$. Note that the angles $\bar{\psi}_{ij}$ are defined up to multiples of π, i.e. although the axis is known, the direction of polarity is undefined at this point. To obtain the ridge pattern in Figure 2H, we rotated the axis of the nematics n_{ij} by $\pi/2$.

To define the hair polarity direction for all boxes, first, we manually set the polarity orientation for some boxes. Then, the polarity direction of the other boxes was iteratively determined by the following condition: the scalar product of the polarity of the current box with the average polarity of all its neighbors with already-defined direction has to be positive. Each arrow on the quantified wing hair patterns was obtained by averaging the polarity vectors over several boxes.

8. Correlations between Ds and Fmi patterns at 32 hAPF

For the patterns in Figure 3K-M, we computed correlations between the averages of two nematic tensors, representing Dachsous polarity and Flamingo polarity, respectively. For each cell α in these wings, we quantified the normalized nematic tensor of Dachsous q_{ds}^{α} and the normalized nematic

tensor of Flamingo $\boldsymbol{q}_{\mathrm{fmi}}^{\alpha}$ as described in Section 5. We divided the images into boxes and defined the total Ds nematic tensor $\boldsymbol{Q}_{\mathrm{ds}}$ and the total Fmi nematic tensor $\boldsymbol{Q}_{\mathrm{fmi}}$ within each box by

$$\boldsymbol{Q}_{\mathrm{ds}} = \sum_{\alpha} \boldsymbol{q}_{\mathrm{ds}}^{\alpha}$$

and

$$\boldsymbol{Q}_{\mathrm{fmi}} = \sum_{\alpha} \boldsymbol{q}_{\mathrm{fmi}}^{\alpha},$$

where the sums run over all cells α within the box. Similarly, we defined the total norm of both polarities by $N_{\mathrm{ds}} = \sum_{\alpha} |\boldsymbol{q}_{\mathrm{ds}}^{\alpha}|$ and $N_{\mathrm{fmi}} = \sum_{\alpha} |\boldsymbol{q}_{\mathrm{fmi}}^{\alpha}|$, respectively, where the norm of any nematic tensor $\boldsymbol{q}$ is defined by $|\boldsymbol{q}| = (q_1{}^2 + q_2{}^2)^{1/2}$.

The angular correlation within each box is defined by

$$a_{\mathrm{ds,fmi}} = \frac{\boldsymbol{Q}_{\mathrm{ds}} : \boldsymbol{Q}_{\mathrm{fmi}}}{|\boldsymbol{Q}_{\mathrm{ds}}||\boldsymbol{Q}_{\mathrm{fmi}}|},$$

where the colon denotes summation over all tensor indices. This angular correlation can take values between -1 and 1. For $a_{\mathrm{ds,fmi}} = 1$, the axes of Ds and Fmi polarity are parallel. For $a_{\mathrm{ds,fmi}} = -1$, the axes of Ds and Fmi polarity are perpendicular.

The combined local nematic order parameter of the cellular Dachsous and Flamingo polarity is defined by

$$c_{\mathrm{ds,fmi}} = \left(\frac{|\boldsymbol{Q}_{\mathrm{ds}}||\boldsymbol{Q}_{\mathrm{fmi}}|}{N_{\mathrm{ds}} N_{\mathrm{fmi}}} \right)^{1/2}.$$

It can take values between 0 and 1. For $c_{\mathrm{ds,fmi}} = 1$, both, Dachsous and Flamingo nematics, are perfectly aligned among cells, respectively. For $c_{\mathrm{ds,fmi}} = 0$, the cellular nematics of at least one of Dachsous or Flamingo are completely random.

9. Wing coordinate system and angle profiles

In order to average or compare wing hair polarity patterns of different wings in Figures 5 and S5, we defined a coordinate system of the Drosophila wing from morphological landmarks (Figure 4G). The origin of the coordinate system is the intersection of the anterior cross vein with vein L4. The x axis goes through the end of L4. The y axis is defined perpendicular to the x axis as in Figure 4G. In order to account for the different sizes of wings, we rescaled all wings with respect to the distance λ_0 of the end of L5 to the x axis. We chose to take this distance as length unit for the numerical solution of Eq. (1).

In order to create the average profiles of wing hair angles (Figures 5C,F,I,L,O,R,U and S5C,F,I,L), we first mapped the quantified wing hair polarity pattern of each wing to our coordinate system. The position of the angle profile is indicated in Figure 4G: it is parallel to the y axis and goes through the end of L5. Furthermore, we rescaled the y axis such that vein positions match those at 32 hAPF. The y coordinates of positions in between two veins were interpolated linearly. After these transformations, normalized wing hair polarity vectors were averaged to obtain average polarity vectors $\boldsymbol{p}$. In the wing hair angle profile plots, we display the angle of these average polarity vectors $\boldsymbol{p}$. Then, the circular standard deviation σ is computed as [S21]

$$\sigma = (-2 \log|\boldsymbol{p}|)^{1/2},$$

where $|\boldsymbol{p}|$ denotes the norm of the polarity vector $\boldsymbol{p}$.

10. Quantification and analysis of wing margin bristle orientation

We quantified the orientation of the bristles along the wing margin using the same algorithm as for the quantification of the wing hair pattern described above (Figure S5M-P). We parameterized the positions along the wing blade margin by the variable s, which is proportional to the margin length passed starting from the posterior indentation at the hinge blade interface (Figure S5M). The variable s reaches its maximal value of $s = 1$ at the anterior indentation at the hinge blade interface. We measured the relative bristle orientation denoted by ψ_b with respect to the margin angle denoted by ψ_m, where the margin angle is defined to point in clockwise orientation around the margin. Note that in order to compare bristle orientation profiles of different wings, we rescaled the position coordinate s in the following way. We mapped the positions of the vein ends of veins L2, L3, L4, and L5 to those of a template wild type wing. In between two vein ends, we linearly interpolated the position coordinate s.

We asked whether Sple over-expression at the wing margin could directly affect bristle orientation. In order to test this, we quantified the margin bristle orientation of *wg>sple* wings, were Sple is over-expressed within a stripe at the wing margin, and compared it to the margin bristle orientation in wild type and in permanent *tub>sple*. The observation that margin bristles in *wg>sple* were mainly oriented as in wild type (Figure S5O) suggested that margin bristle orientation is largely independent of Sple over-expression at the wing margin. Together with our observation that wing hairs close to the margin pointed always in similar directions as close margin bristles, these findings indicate that margin bristle orientations could be coupled to the Core PCP system at the margin, independent of Sple over-expression. These considerations motivate the boundary conditions of our physical theory (Supplemental Theoretical Procedures, Section 2).

11. Quantification of flow fields in the pupal fly wing using particle image velocimetry (PIV)

In this section, we describe how the flow fields shown in Movie S3 and their spatial averages shown in Figure S4O,P were obtained. We start from a series of digital images with pixel intensities $I_k(\boldsymbol{r})$, where the integer k denotes the number of the image and the vector $\boldsymbol{r}$ denotes a pixel position. In order to determine the local displacement field of tissue between two consecutive images, k and $k + 1$, we divided the images into boxes of 128x128 pixels (at a spatial resolution of 0.2 µm per pixel). Here, we label each box ij by a column index i and a row index j. We determined the most likely displacement of a given box ij between images k and $k + 1$ as follows. For a given integer displacement vector $\Delta\boldsymbol{r}$, we correlated the pixel intensities within box ij in image k with the pixel intensities within the box ij shifted by vector $\Delta\boldsymbol{r}$ in image $k + 1$. More precisely, to obtain the most likely displacement vector $\Delta\boldsymbol{r}$ of box ij, we maximized the following covariance function $c(\Delta\boldsymbol{r}; k, k + 1, ij)$:

$$c(\Delta\boldsymbol{r}; k, k+1, ij) = \frac{\langle I_k(\boldsymbol{r})I_{k+1}(\boldsymbol{r}+\Delta\boldsymbol{r})\rangle_{ij} - \langle I_k(\boldsymbol{r})\rangle_{ij}\langle I_{k+1}(\boldsymbol{r}+\Delta\boldsymbol{r})\rangle_{ij}}{\left[\left(\langle I_k^2(\boldsymbol{r})\rangle_{ij} - \langle I_k(\boldsymbol{r})\rangle_{ij}^2\right)\left(\langle I_{k+1}^2(\boldsymbol{r}+\Delta\boldsymbol{r})\rangle_{ij} - \langle I_{k+1}(\boldsymbol{r}+\Delta\boldsymbol{r})\rangle_{ij}^2\right)\right]^{1/2}}.$$

In this equation, the averaging brackets define the average of any position-dependent quantity $q(\boldsymbol{r})$ over all pixels positions $\boldsymbol{r}$ of box ij:

$$\langle q(\boldsymbol{r})\rangle_{ij} = \frac{1}{N}\sum_{\boldsymbol{r}} q(\boldsymbol{r}).$$

Here, the sum runs over all N integer pixel positions within box ij. For each box ij and each image pair $k, k+1$ of the image sequence, we maximized the covariance $c(\Delta \boldsymbol{r}; k, k+1, ij)$ to obtain the most likely box displacement vector $\Delta \boldsymbol{r}_k(ij)$. For this maximization, we varied $\Delta \boldsymbol{r}$ by 15 pixels in positive and negative x and y direction, respectively.

The space- and time-dependent velocity field $\mathbf{v}_k(ij)$ was obtained by dividing all displacement vectors by the time interval Δt_k between images k and $k+1$: $\mathbf{v}_k(ij) = \Delta \boldsymbol{r}_k(ij)/\Delta t_k$. The shear field was obtained from the velocity gradient. For a given box ij, the derivative of the velocity field with respect to x was approximated by $[\mathbf{v}_k(i+1, j) - \mathbf{v}_k(i-1, j)]/2b_x$, where b_x is the width of the boxes. Similarly, the derivative of the velocity field with respect to y was approximated by $[\mathbf{v}_k(i, j+1) - \mathbf{v}_k(i, j-1)]/2b_y$, where b_y is the height of the boxes. Then, the shear nematic for a given box is the traceless, symmetric part of the velocity gradient tensor. In Movie S3, velocity field and shear field where smoothened by averaging over a time window of ca. 90 minutes.

The plots in Figure S4O,P were created as follows. For a given time (i.e. for a given image pair $k, k+1$), the velocity field and the shear field were averaged over all boxes belonging to the wing blade. Then, the average velocity vector and the average shear nematic were respectively projected onto the direction defined by vein L3, pointing distally.

Supplemental Theoretical Procedures

Here, we present the details of our theoretical analysis of Core PCP reorientation during pupal stages until the start of wing hair outgrowth.

We treat the wing epithelium on a coarse-grained level as a polar fluid [S22] with two polarity vector fields: $\boldsymbol{p}$ representing Core PCP and $\boldsymbol{q}$ representing Fat PCP. Both polarity fields are normalized to one: $|\boldsymbol{p}| = |\boldsymbol{q}| = 1$. We focused on the dynamics of the polarity field $\boldsymbol{p}$ imposing the flow field of the tissue and the polarity field $\boldsymbol{q}$.

1. Bulk dynamics

We used the following expression for an effective distortion free energy of the polarity field $\boldsymbol{p}$:

$$F_{\text{total}} = \int \left[\frac{K}{2}\partial_i p_j \partial_i p_j - Z p_i q_i + \frac{\Lambda_\parallel}{2} p_i p_i\right] \mathrm{d}^2 x + F_{\text{boundary}}, \tag{S1}$$

where $i, j \in \{x, y\}$ are dimension indices and Einstein convention is used. The symbol K denotes the elastic coefficient for neighbor coupling of the polarity field $\boldsymbol{p}$. It is positive. The symbol Z denotes the elastic coefficient that describes the coupling between $\boldsymbol{p}$ and $\boldsymbol{q}$. For positive Z, the polarity fields $\boldsymbol{p}$ and $\boldsymbol{q}$ are preferentially oriented in the same direction. The Lagrange multiplier $\Lambda_\parallel$ ensures the normalization of $\boldsymbol{p}$. The boundary term F_{boundary} is discussed below. We used the following flux force relation for the time derivative of $\boldsymbol{p}$:

$$\frac{\partial p_i}{\partial t} = -\frac{1}{\gamma_1}\frac{\delta F_{\text{total}}}{\delta p_i} - \nu \tilde{u}_{ij} p_j, \tag{S2}$$

where we ignore for simplicity the convective and the corotational term in the time derivative of $\boldsymbol{p}$. The symbols γ_1 and ν denote phenomenological coefficients and γ_1 is positive. The term $\delta F_{\text{total}}/\delta p_i$ represents the functional derivative of the distortion free energy with respect to the polarity field $\boldsymbol{p}$. The tensor $\tilde{u}_{ij} = \left(u_{ij} + u_{ji} - \delta_{ij}u_{ll}\right)/2$ is the traceless symmetric part of the velocity gradient u_{ij}. From Eqs. (S1) and (S2) follows the following dynamic equation for the polarity field $\boldsymbol{p}$ in the bulk

$$\frac{\partial p_i}{\partial t} = -\nu\tilde{u}_{ij}p_j + \zeta q_i + \kappa\partial_j\partial_j p_i - \lambda_\parallel p_i, \tag{S3}$$

where we defined $\kappa = K/\gamma_1$, $\zeta = Z/\gamma_1$, and $\lambda_\parallel = \Lambda_\parallel/\gamma_1$. In deriving Eq. (S3), we assumed homogeneous K. However, inhomogeneity in κ can still be accounted for by inhomogeneity in γ_1. From Eq. (S3) follows Eq. (1) in the main text, where the angles ψ and ϕ of the polarity fields $\boldsymbol{p}$ and $\boldsymbol{q}$ are defined by

$$\boldsymbol{p} = \begin{pmatrix} \cos\psi \\ \sin\psi \end{pmatrix} \qquad \text{and} \qquad \boldsymbol{q} = \begin{pmatrix} \cos\phi \\ \sin\phi \end{pmatrix},$$

respectively. Furthermore, the angle θ of the shear axis is defined by

$$\cos(2\theta) = \frac{\tilde{u}_{xx}}{k}$$

$$\sin(2\theta) = \frac{\tilde{u}_{xy}}{k},$$

where the shear rate k is defined by $k = \left(\tilde{u}_{xx}^{\;2} + \tilde{u}_{xy}^{\;2}\right)^{1/2}$. The x and y axes in these definitions are defined by the wing coordinate system shown in Figure 4G.

Note that time-dependent Sple over-expression was achieved by exposing the flies to varying temperatures during development. However, it is known that the speed of developmental processes is temperature-dependent. In order to treat all conditions of Sple over-expression studied in a unified description, all times and rates in our theoretical description relate to the development at 25ºC.

2. Boundary Conditions

The boundary in our numerical solutions was defined by the margin of the wing blade. However, in order to close the boundary, we connected the two indentations at the hinge-blade (HB) interface by a straight line.

Motivated by our measurements of margin bristle directions (Supplemental Experimental Procedures, Section 10), we impose the following boundary conditions. We introduce an effective potential f_b for the bristle direction ψ_b at each point of the boundary. This effective potential depends on the bristle direction relative to the margin $\psi_b - \psi_m$. Furthermore, the effective potential f_b is the same for wild type tissue and for tissue over-expressing Sple. In addition, the bristle direction ψ_b is coupled by an elastic element to the local Core PCP direction ψ_0 at the boundary. The contributions of the boundary to the effective distortion free energy read

$$F_{\text{boundary}} = \oint [f_b(\psi_b - \psi_m) - \text{C}\cos(\psi_0 - \psi_b)]\mathrm{d}l, \tag{S4}$$

where the contour integral goes along the entire boundary. The positive coefficient C describes the elasticity of the coupling between Core PCP at the margin and bristle direction.

The functional form of f_b was fixed by the following considerations. First, for simplicity, $f_b(\psi_b - \psi_m)$ should be symmetric around $\psi_b - \psi_m = \pi/2$ corresponding to the absence of chiral

terms at the boundary. Second, we never observed bristles pointing into the blade. Because of this, we chose to penalize the corresponding angle differences $\psi_b - \psi_m$. A simple generic form of f_b that is consistent with these two aspects and includes the two lowest Fourier modes is given by

$$f_b(\psi_b - \psi_m) = B[-\sin(\psi_b - \psi_m) + a\cos(2[\psi_b - \psi_m])], \tag{S5}$$

where B and a are elastic coefficients with $B > 0$. For $a < -0.25$, the potential f_b possesses two minima within the relevant angle interval $\psi_b - \psi_m = 0 \dots \pi$. Otherwise it possesses only a single minimum within this interval, which is located at $\psi_b - \psi_m = \pi/2$.

The boundary conditions follow from the condition of force balances $\delta F_{\text{total}} = 0$ at the boundary. Using Eqs. (S1) and (S4), one obtains:

$$\frac{df_b(\psi_b - \psi_m)}{d\psi_b} = C\sin(\psi_0 - \psi_b) \tag{S6}$$

and

$$C\sin(\psi_0 - \psi_b) = -Kn_i\partial_i\psi, \tag{S7}$$

where n_i is the normalized local normal vector to the boundary pointing outside.

In order to reduce the number of unknown parameters, we assume a strong coupling $C \gg B$ and $C \gg Ba$ between Core PCP at the margin and the bristle orientation, here. Then, from Eqs. (S5)-(S7) follows $|\psi_0 - \psi_b| \ll 1$ and the following boundary condition:

$$n_i\partial_i\psi = \frac{B}{K}[\cos(\psi_0 - \psi_m) + 2a\sin(2[\psi_0 - \psi_m])], \tag{S8}$$

which holds in each point on the boundary. In our numerical solutions of Eq. (1) in the main text, we used Eq. (S8) as boundary condition with position-dependent parameter values B/K and a.

In order to determine the parameter values for B/K and a in Eq. (S8), we quantified not only the bristle angle ψ_b but also the wing hair angle ψ_w at a distance w away from the margin (Figure S5M). We plot $\psi_b - \psi_w$ over $(\psi_b + \psi_w)/2 - \psi_m$. To first order in w and in $\psi_b - \psi_w$, one obtains from Eq. (S8), that

$$\psi_b - \psi_w = \frac{\frac{wB}{K}\left[\cos\left(\frac{(\psi_b + \psi_w)}{2} - \psi_m\right) + 2a\sin\left(2\left[\frac{(\psi_b + \psi_w)}{2} - \psi_m\right]\right)\right]}{1 + \frac{wB}{2K}\left[\sin\left(\frac{(\psi_b + \psi_w)}{2} - \psi_m\right) - 4a\cos\left(2\left[\frac{(\psi_b + \psi_w)}{2} - \psi_m\right]\right)\right]}. \tag{S9}$$

By fits of Eq. (S9) to our data, we found that the angle differences $\psi_b - \psi_w$ are well described by two parameter sets. One parameter set describes the margin regions posterior to L3 (between $s = 0$ and $s \approx 0.55$) and the other parameter set describes the margin regions anterior to L3 (between $s \approx 0.55$ and $s = 1$). The fit for the first parameter set is shown in Figure S5N, where we obtained $w_{\text{eff}}B/K = 2.9$ and $a = -0.23$. For the second parameter set between $s \approx 0.55$ and $s = 1$, we obtained $w_{\text{eff}}B/K = 0.69$ and $a = -0.32$. We adjusted w such that the final boundary polarity in the numerical solution of the wild type case yields a good fit to the measured bristle orientations (Figure S5P). Now, we list the resulting coefficients B/K and a used for all numerical solutions shown in this article. For margin regions posterior to L3 (between $s = 0$ and $s \approx 0.55$), we set $B_P/K = 70/\lambda_0$ and $a_P = -0.23$. For margin regions anterior to L3 (between $s \approx 0.55$ and $s = 1$), we set $B_A/K = 16/\lambda_0$ and $a_A = -0.32$. For the straight line, which cuts the wing at the HB interface, we use open boundary conditions, which result from Eq. (S8) for $B = 0$. With our model, we could also qualitatively account

for the bristle orientations of the other conditions (data not shown). In the numerical solutions shown in Figures 5 and S5, the direction of margin bristles (which corresponds to the polarity at the wing margin) is indicated by green arrows. Margin regions where the anterior boundary condition (first parameter set) was used are marked by darker arrows.

3. Fits to one-dimensional wing hair angle profiles

In order to determine characteristic length scale parameters of Core PCP reorientation, we fit solutions of Eq. (1) reduced to one dimension (independent on the x coordinate) to quantified wing hair angle profiles (data not shown). In order to compute the stationary solutions $\psi(y)$ of Eq. (1) in one dimension, we used the simplified shear field and the simplified Fat PCP direction field described in the main text, but without the flips around the veins. Thus, we calculated solutions $\psi(y)$ of the ordinary differential equation

$$0 = \frac{k\nu}{\kappa}\sin(2\psi) - \frac{\zeta}{\kappa}\sin(\psi - \phi) + \frac{\mathrm{d}^2\psi}{\mathrm{d}y^2}, \tag{S10}$$

for homogeneous parameter values $k\nu/\kappa$ and ζ/κ, and for

$$\phi = \begin{cases} -\dfrac{\pi}{2} & \text{for } y \leq y_{\mathrm{L3}} \\ +\dfrac{\pi}{2} & \text{for } y > y_{\mathrm{L3}} \end{cases},$$

where y_{L3} corresponds to the position of the L3 vein. We solved Eq. (S10) separately for $y \leq y_{\mathrm{L3}}$ and for $y \geq y_{\mathrm{L3}}$, yielding the solutions $\psi_-(y)$ and $\psi_+(y)$, respectively. As interface conditions, we used

$$\psi_-(y_{\mathrm{L3}}) = \psi_+(y_{\mathrm{L3}}) \qquad \text{and} \qquad \frac{\mathrm{d}\psi_-(y_{\mathrm{L3}})}{\mathrm{d}y} = \frac{\mathrm{d}\psi_+(y_{\mathrm{L3}})}{\mathrm{d}y},$$

which follow from the condition of local force balance at y_{L3} using Eq. (S1).

Solutions to Eq. (S10) for constant $\phi = \pm\pi/2$ can be obtained analytically. In the special case $\zeta = 0$, but $k\nu \neq 0$, the solutions are

$$\psi(y) = \frac{n\pi}{2} + \mathrm{am}\left(\frac{y - y_0}{m\lambda}\bigg| m\right),$$

where the integer n is even for $k\nu > 0$ and odd for $k\nu < 0$. The real numbers y_0 and m are the integration constants and the symbol λ denotes the characteristic length scale of the shear alignment, which is defined by

$$\lambda = \left(\frac{\kappa}{2|k\nu|}\right)^{1/2}. \tag{S11}$$

In the above equation, the function $\mathrm{am}(x|m)$ represents the inverse of the incomplete elliptic integral of the first kind [S23].

Similarly, for $k\nu = 0$, but $\zeta \neq 0$, the solutions of Eq. (S10) can be expressed as

$$\psi(y) = \phi + n\pi + 2\,\mathrm{am}\left(\frac{y - y_0}{m\mu}\bigg| m\right),$$

where the integer n is even for $\zeta < 0$ and odd for $\zeta > 0$. Again, the real numbers y_0 and m are the integration constants and the symbol μ denotes the characteristic length scale of the coupling to Fat PCP. It is defined by

$$\mu = \left(\frac{\kappa}{|\zeta|}\right)^{1/2}. \tag{S12}$$

In order to obtain the length scale parameters λ and μ, we fit our full solution of Eq. (S10) to one-dimensional wing hair angle profiles plotted along the line shown in Figure 4G. Therefore, consistent with the idea that the parameter values $k\nu$, ζ, and κ are different between wild type-like tissue and in tissue over-expressing Sple, we also chose different values of the characteristic length scales λ and μ in both cases. For wild type-like tissue, we denote them by λ_{wt} and μ_{wt} and for tissue over-expressing Sple, we denote them by λ_{so} and μ_{so}. Depending on whether Sple is over-expressed or not at the time of wing hair outgrowth, we used the appropriate characteristic length scales in our full analytical solution for Eq. (S10). For over-expression of Sple only posteriorly (i.e. in the permanent and late *en(105)>sple* cases), we combined the solution $\psi_A(y)$ with wild type parameters for $y \geq y_{AP}$ with the solution $\psi_P(y)$ with Sple over-expression parameters for $y \leq y_{AP}$. The parameter y_{AP}, which corresponds to the position of the AP boundary, is a fit parameter. We used the following interface conditions

$$\psi_P(y_{AP}) = \psi_A(y_{AP}) \qquad \text{and} \qquad \frac{\mathrm{d}\psi_P(y_{AP})}{\mathrm{d}y} = \frac{\mathrm{d}\psi_A(y_{AP})}{\mathrm{d}y},$$

which follow from the condition of local force balance at y_{AP} using Eq. (S1).

The fit parameters used were the length scales λ_{wt}, μ_{wt}, λ_{so}, and μ_{so}; and two integration constants that were not fixed by the interface conditions. In addition, in the fits for the permanent and late *en(105)>sple* cases, the parameter y_{AP} was also varied. As discussed in Section 5 below, the constraints $\lambda_{\mathrm{so}}/\mu_{\mathrm{so}} = \sqrt{2}$ and $\mu_{\mathrm{wt}} \to \infty$ were used for the fits. Furthermore, consistent with our discussion below, we assumed for our fits that $k\nu_{\mathrm{wt}} < 0$, $\zeta_{\mathrm{wt}} = 0$, $k\nu_{\mathrm{so}} < 0$, and $\zeta_{\mathrm{so}} < 0$. However, we noticed, that our fits would also be consistent with the wing hair data for $k\nu_{\mathrm{so}} > 0$, and $\zeta_{\mathrm{so}} = 0$. We discuss this alternative possibility below (see Section 6). Note that for the fit of the permanent *tub>sple* case, we only fit the region with $y > -0.6$, because around the distal end of L5 there is a topological defect in the wing hair pattern of these wings. Therefore, the assumption of homogeneity in x direction is not fulfilled close to this point.

We found that for all cases analyzed, the quantified wing hair patterns are largely well described by stationary solutions of Eq. (S10) (data not shown). The obtained characteristic length scales λ_{wt} and μ_{so} are listed in Table S1 for each case. However, for the wild type case, we could not obtain sensible length scales, since in this case, the quantified wing hair angle profile is mainly flat.

The obtained parameter values are largely consistent among the different cases. We found that on average, $\lambda_{\mathrm{wt}} = 0.07\lambda_0$ and $\mu_{\mathrm{so}} = 0.16\lambda_0$. The only variation occurs in the characteristic length scale μ_{so} for the permanent *tub>sple* case. We suggest that this variation is due to an effect of veins to align Core PCP parallel to their local axis. Since this effect is very prominent around vein L4 ($y = 0$) in the permanent *tub>sple* case, it considerably distorts the obtained length scale μ_{so} in this case. We therefore excluded this case from the above averages.

4. Numerical study of PCP orientation dynamics

We numerically solved Eq. (1) using a finite difference method with Euler steps. We used squared boxes with a side length of $0.05\lambda_0$. In order to display polarity patterns, we coarse-grained the normalized polarity vectors within bigger boxes, which contain 4 by 4 of the smaller boxes.

We solved Eq. (1) on a domain that corresponds to the blade of a wild type wing at 32 hAPF. We cut the blade from the hinge by a straight line exactly between the two indentations at the hinge blade interface. The boundary conditions used are described by Eq. (S8) above with the parameter values listed in the same section.

The orientation field of shear (θ) and the direction field of Fat PCP (ϕ) used are defined in the main text (below Eq. (1)). The flips of the ϕ field around the veins L3, L4, and L5 were defined in the following way. In a region anterior to vein L3 with a width that corresponds to 4 to 5 cells, the assumed Ds polarity points posteriorly ($\phi = -\pi/2$). Furthermore, in regions posterior to veins L3 and L4 with a width that corresponds to 3 to 4 cells; and in a region posterior to vein L5 with a width that corresponds to 2 to 3 cells, the assumed Ds polarity points anteriorly ($\phi = +\pi/2$).

We used simplified initial conditions, which were based on quantified Core PCP patterns. The generic form of our simplified initial conditions was given by position-independent angles ψ_P^{IC} and ψ_A^{IC} in the regions corresponding to anterior and posterior compartment and a cubic spline interpolating in between. Its functional form is defined by

$$\psi^{\text{IC}}(x,y) = \begin{cases} \psi_P^{\text{IC}} & \text{for } y \leq y^{\text{IC}} - w^{\text{IC}}/2 \\ \psi_P^{\text{IC}} + \left(\psi_A^{\text{IC}} - \psi_P^{\text{IC}}\right)(3 - 2\bar{y})\bar{y}^2 & \text{for } y^{\text{IC}} - w^{\text{IC}}/2 < y \leq y^{\text{IC}} + w^{\text{IC}}/2 \\ \psi_A^{\text{IC}} & \text{for } y^{\text{IC}} + w^{\text{IC}}/2 < y, \end{cases}$$

where $\bar{y} = (y - y^{\text{IC}})/w^{\text{IC}} + 1/2$. The parameters y^{IC} and w^{IC} denote the center position and the width of the interpolating region, respectively. In our numerical solutions, we set $y^{\text{IC}} = 0.1\lambda_0$ and $w^{\text{IC}} = 0.3\lambda_0$. The predicted final polarity patterns are largely independent of w^{IC} and only the patterns of the early and permanent *en(105)>sple* cases depend on y^{IC}. The value of y^{IC} was adjusted such that in the early *en(105)>sple* case, the position of the bending region for the quantified wing hair patterns is matched by the predicted final polarity pattern.

The angles ψ_P^{IC} and ψ_A^{IC} were chosen as follows. For the initial condition shown in Figure 4J, we chose $\psi_P^{\text{IC}} = -0.25\pi$ and $\psi_A^{\text{IC}} = 0.25\pi$, which was based on quantified Core PCP in wild type wings grown at 25ºC at 16 hAPF [S20]. For the initial condition shown in Figure 4L, we chose $\psi_P^{\text{IC}} = -1.25\pi$ and $\psi_A^{\text{IC}} = 0.25\pi$, which was based on quantified Core PCP in permanent *en(105)>sple* wings grown at 25ºC at 16 hAPF. For the initial condition shown in Figure 4K, we chose $\psi_P^{\text{IC}} = -1.25\pi$ and $\psi_A^{\text{IC}} = -0.75\pi$, which corresponds to the opposite pattern than the wild type initial condition shown in Figure 4J.

5. Determination of bulk parameter values

We proceeded as follows to fix the parameters for the bulk dynamics to the values listed in Table S2. First, for wild type tissue, we set $\zeta_{\text{wt}} = 0$. This was motivated by the wing hair patterns shown in Figure S3L-Q as explained in the main text. As a consequence, according to Eq. (S12), the characteristic length scale μ_{wt} is infinitely large. Using this constraint, we obtained the characteristic length scale $\lambda_{\text{wt}} = 0.07\lambda_0$ from the one-dimensional fits to the early *en(105)>sple* and *tub>sple* cases (see Table S1 and Section 3).

In order to determine the parameter value for $k\nu_{\text{wt}}$, we fit a numerical solution of Eq. (1) to the quantified time-dependent Core PCP pattern in the whole wing shown in Figure 1 (Movie S4-8). To

this end, we proceeded as follows. The Core PCP data shown in Figure 1 consists of the quantified Core PCP nematic for each cell, where one entire wing was segmented each hour during the time interval between 16 hAPF and 32 hAPF. For the numerical solutions, we started from the initial condition given by the coarse-graining the quantified pattern at 16 hAPF within the bigger boxes. Since only the local axis of Core PCP was quantified, we fixed the vector directions to match the known wild type Core PCP pattern at 16 hAPF [S20]. Then, Eq. (1) was solved with varying parameter kv_{wt}, where in each case, the parameter κ_{wt} was fixed using the known length scale λ_{wt} and Eq. (S11). For each value kv_{wt}, we computed the deviation χ^2 of the numerical solution to the time-dependent quantified Core PCP pattern, which is defined by

$$\chi^2 = \frac{1}{N_t N_b} \sum_{t,i} \left[1 - \cos\left(2\left[\psi^i(t) - \psi_q^i(t)\right]\right)\right],$$

where the sum run over all $N_t = 16$ time points t of the Core PCP quantification between 17 hAPF and 32 hAPF and over all N_b small boxes labeled by i. The polarity angle pattern of the numerical solution is denoted by $\psi^i(t)$ and the angle of the coarse-grained quantified Core PCP pattern within each box is given by $\psi_q^i(t)$. By definition, χ^2 can take only values between zero and two. For $\chi^2 = 0$, both polarity patterns are always parallel and for $\chi^2 = 2$, both polarity patterns are always perpendicular to each other. By varying the value of kv_{wt}, we found that the deviation χ^2 is minimal for $kv_{wt} = -0.1 \text{ h}^{-1}$ (Movie S4-8).

For tissue over-expressing Sple, we found that all wing hair patterns could be reproduced if the coupling coefficient to Fat PCP ζ_{so} was negative and $|\zeta_{so}|$ was at least two to three times larger than $|kv_{so}|$. Thus, whenever $|\zeta_{so}|$ was large enough, the actual value of kv_{so} had only little influence on the results of our numerical solutions. In Figure 5 (model A), we chose $kv_{so} = kv_{wt}$. We found that under this assumption, all wing hair patterns could largely be reproduced for $\zeta_{so} \lesssim -0.4 \text{ h}^{-1}$. In order to keep κ_{so} as close as possible to κ_{wt}, we chose $|\zeta_{so}|$ as small as possible (see also Eqs. (S11) and (S12)). We chose $\zeta_{so} = -0.4 \text{ h}^{-1}$. From Eqs. (S11) and (S12) follows that

$$\frac{\lambda_{so}}{\mu_{so}} = \left(\frac{|\zeta_{so}|}{2|kv_{so}|}\right)^{1/2}.$$

With the parameter values for kv_{so} and ζ_{so} follows that $\lambda_{so}/\mu_{so} = \sqrt{2}$. Using this constraint, we fitted the one-dimensional hair angle profiles for the late and permanent Sple over-expression and obtained $\mu_{so} = 0.16\lambda_0$ (see Table S1 and Section 3). Then, κ_{so} was fixed using the known length scale μ_{so} and Eq. (S12).

6. Alternative model for the effects of Sple over-expression

Motivated by results of our fits to one-dimensional wing hair angle profiles, we also discussed in our analysis the possibility that a coupling to the Fat PCP field plays no role at all, i.e. $\zeta_{wt} = \zeta_{so} = 0$ (Figure S5A-L, model B). Instead, Sple over-expression changes the value of kv to a positive value $kv_{so} > 0$. Under these assumptions, the fits to the one-dimensional wing hair angle profiles yield $\lambda_{wt} = 0.07\lambda_0$ and $\lambda_{so} = 0.14\lambda_0$ (data not shown).

We numerically solved Eq. (1) with $kv_{wt} = -0.1 \text{ h}^{-1}$ and fixed the value for κ_{wt} using Eq. (S11). As result of our numerical solutions, for the late *tub>sple* and *en(105)>sple* cases, the predicted

final polarity patterns clearly disagree with the quantified wing hair patterns (Figure S5A-C,G-I). We tested this for many values of kv_{so}, where for given value of kv_{so}, we fixed κ_{so} using Eq. (S11). For the numerical solutions shown in Figure S5A-L, we used the parameter value of $kv_{so} = 0.1\ \mathrm{h}^{-1}$.

For the permanent *tub>sple* case, the final polarity pattern matches the quantified wing hair pattern only badly (Figure S5D-F). However surprisingly, for the permanent *en(105)>sple* case, the predicted final polarity patterns largely matches the quantified wing hair pattern (Figure S5J-L). Note that for the wild type case and the early *tub>sple* and *en(105)>sple* cases, the numerical solutions are the same for both models, because we used the same wild type parameter values kv_{wt}, ζ_{wt}, and κ_{wt}.

To sum up, we found that a scenario where Sple over-expression flips the sign of kv to positive but does not reinforce a coupling ζ_{so} to Fat PCP clearly fails to predict the wing hair patterns in the late over-expression experiments.

Supplemental References

S1.   Bryant, P.J., Huettner, B., Held, L.I., Jr., Ryerse, J., and Szidonya, J. (1988). Mutations at the fat locus interfere with cell proliferation control and epithelial morphogenesis in Drosophila. Developmental biology *129*, 541-554.

S2.   Gubb, D., Green, C., Huen, D., Coulson, D., Johnson, G., Tree, D., Collier, S., and Roote, J. (1999). The balance between isoforms of the prickle LIM domain protein is critical for planar polarity in Drosophila imaginal discs. Genes Dev *13*, 2315-2327.

S3.   Jones, K.H., Liu, J., and Adler, P.N. (1996). Molecular analysis of EMS-induced frizzled mutations in Drosophila melanogaster. Genetics *142*, 205-215.

S4.   Matakatsu, H., and Blair, S.S. (2006). Separating the adhesive and signaling functions of the Fat and Dachsous protocadherins. Development *133*, 2315-2324.

S5.   Wolff, T., and Rubin, G.M. (1998). Strabismus, a novel gene that regulates tissue polarity and cell fate decisions in Drosophila. Development *125*, 1149-1159.

S6.   Eugster, C., Panakova, D., Mahmoud, A., and Eaton, S. (2007). Lipoprotein-heparan sulfate interactions in the Hh pathway. Developmental cell *13*, 57-71.

S7.   Mao, Y., Rauskolb, C., Cho, E., Hu, W.L., Hayter, H., Minihan, G., Katz, F.N., and Irvine, K.D. (2006). Dachs: an unconventional myosin that functions downstream of Fat to regulate growth, affinity and gene expression in Drosophila. Development *133*, 2539-2551.

S8.   Huang, J., Zhou, W., Dong, W., Watson, A.M., and Hong, Y. (2009). Directed, efficient, and versatile modifications of the Drosophila genome by genomic engineering. Proc Natl Acad Sci U S A *106*, 8284-8289.

S9.   Strutt, D.I. (2001). Asymmetric localization of frizzled and the establishment of cell polarity in the Drosophila wing. Molecular cell *7*, 367-375.

S10.   Brittle, A., Thomas, C., and Strutt, D. (2012). Planar Polarity Specification through Asymmetric Subcellular Localization of Fat and Dachsous. Curr Biol.

S11.   Strutt, D., and Strutt, H. (2007). Differential activities of the core planar polarity proteins during Drosophila wing patterning. Dev Biol *302*, 181-194.

S12.   Bischof, J., Maeda, R.K., Hediger, M., Karch, F., and Basler, K. (2007). An optimized transgenesis system for Drosophila using germ-line-specific phiC31 integrases. Proceedings of the National Academy of Sciences of the United States of America *104*, 3312-3317.

S13.   Venken, K.J., Schulze, K.L., Haelterman, N.A., Pan, H., He, Y., Evans-Holm, M., Carlson, J.W., Levis, R.W., Spradling, A.C., Hoskins, R.A., et al. (2011). MiMIC: a highly versatile transposon insertion resource for engineering Drosophila melanogaster genes. Nat Methods *8*, 737-743.

S14.   McGuire, S.E., Le, P.T., Osborn, A.J., Matsumoto, K., and Davis, R.L. (2003). Spatiotemporal rescue of memory dysfunction in Drosophila. Science *302*, 1765-1768.

S15.   Sagner, A., Merkel, M., Aigouy, B., Gaebel, J., Brankatschk, M., Julicher, F., and Eaton, S. (2012). Establishment of global patterns of planar polarity during growth of the Drosophila wing epithelium. Curr. Biol. *22*, 1296-1301.

S16.   Preibisch, S., Saalfeld, S., and Tomancak, P. (2009). Globally optimal stitching of tiled 3D microscopic image acquisitions. Bioinformatics *25*, 1463-1465.

S17.   Rizk, A., Paul, G., Incardona, P., Bugarski, M., Mansouri, M., Niemann, A., Ziegler, U., Berger, P., and Sbalzarini, I.F. (2014). Segmentation and quantification of subcellular structures in fluorescence microscopy images using Squassh. Nature protocols *9*, 586-596.

S18.   Classen, A.K., Aigouy, B., Giangrande, A., and Eaton, S. (2008). Imaging Drosophila pupal wing morphogenesis. Methods Mol Biol *420*, 265-275.

S19.   Neff, D., Hogan, J., and Collier, S. (2012). Cuticle refraction microscopy: a rapid and simple method for imaging Drosophila wing topography, an alternative readout of wing planar cell polarity. Methods Mol Biol *839*, 43-52.

S20.   Aigouy, B., Farhadifar, R., Staple, D.B., Sagner, A., Roper, J.C., Julicher, F., and Eaton, S. (2010). Cell flow reorients the axis of planar polarity in the wing epithelium of Drosophila. Cell *142*, 773-786.

S21.   Friedmann, I., Michaels, L., and Bird, E.S. (1971). Crystalline strucutes in lymphocytes. J Pathol *105*, 289-290.

S22.   Friedman.I, and Bird, E.S. (1971). Ciliary Structure, Ciliogenesis, Microvilli - (Electron Microscopy of Mucosa of Upper Respiratory Tract). Laryngoscope *81*, 1852-&.

S23.   Byrd, P.F., and Friedman, M.D. (1971). Handbook of elliptic integrals for engineers and scientists, (Springer-Verlag).